

Jesse Peltoniemi

FABRICATION OF FIBER BRAGG GRATINGS USING INTERFEROMETRIC METHODS FOR SENSING APPLICATIONS

Master of Science Thesis
Faculty of Engineering and Natural Sciences
Examiners: Adj. Prof, Regina Gumenyuk
PhD, R&D engineer, Andrei Fedotov
March 2025

ABSTRACT

Jesse Peltoniemi: Fabrication of Fiber Bragg Gratings Using Interferometric Methods For Sensing Applications
Master of Science Thesis
Tampere University
Masters's Programme in Engineering and Natural Sciences
March 2025

Fiber Bragg gratings (FBGs) are highly sensitive optical components widely used for precise measurements of temperature, strain, and pressure. Their advantages—such as high accuracy, immunity to electromagnetic interference, multiplexing capabilities, and robustness in harsh environments—make them ideal for structural health monitoring, aerospace, and medical sensing applications. In structural monitoring, FBGs detect strain variations in bridges and buildings, providing real-time data to prevent failures, while in medical applications, they enable minimally invasive pressure and temperature sensing for diagnostics and treatment.

This work, conducted at Modulight Corporation, focused on developing and optimizing the FBG fabrication process. All key stages were examined, including pre-inscription, grating inscription mechanisms, design parameter interactions affecting sensor performance, and post-inscription processing and characterization. The developed process demonstrated reliable and consistent FBG fabrication, with scalability and adaptability for diverse industrial applications. Further developments are necessary to optimize the fabrication process for specialized applications, such as single-frequency laser systems.

Additionally, this study evaluated the properties of in-house inscribed large-diameter FBGs for temperature sensing applications. The fabricated FBGs exhibited promising performance, achieving a temperature measurement accuracy of $\sigma_{T'} = 0.55^\circ\text{C}$, closely matching the 0.55°C , the accuracy of a commercial FBG. This similarity in accuracy indicates that the in-house fabricated FBGs can perform at a level comparable to commercially available sensors.

Overall, this work successfully optimized a systematic and reliable FBG fabrication process, which has now been implemented at Modulight Corporation. Furthermore, the results highlight the potential of large-diameter FBGs for robust and precise sensing applications.

Keywords: optical fiber, fiber Bragg grating, photosensitivity, FBG fabrication, FBG sensor

The originality of this thesis has been checked using the Turnitin OriginalityCheck service.

TIIVISTELMÄ

Jesse Peltoniemi: Braggin kuituhilojen valmistus hyödyntäen interferometrisiä menetelmiä mittauksistarkoituksiin
Diplomityö
Tampereen yliopisto
Tekniikan ja luonnontieteiden diplomiohjelma
Maaliskuu 2025

Braggin kuituhila (Fiber Bragg Grating, FBG) on erittäin herkkä optinen komponentti, jota voidaan käyttää lämpötilan, rasituksen ja paineen mittaamiseen. Niiden korkea mittaustarkkuus, häiriönsieto sähkömagneettisissa ympäristöissä sekä kestävyys vaativissa olosuhteissa tekevät niistä ihanteellisia rakenteiden kunnonvalvontaan, ilmailualan sovelluksiin ja lääketieteelliseen hoitoihin. Esimerkiksi rakennusten ja siltojen rakenteellisessa valvonnassa FBG-hilat havaitsevat venymämuutoksia reaaliaikaisesti, mikä auttaa ehkäisemään vaurioita. Lääketieteessä niitä voidaan hyödyntää ei-invasiivisissa paineen ja lämpötilan mittauksissa diagnostiikkaa ja hoitoa varten.

Tämä työ toteutettiin Modulight Oyj:llä ja siinä keskityttiin FBG:eiden valmistusprosessin kehittämiseen ja optimointiin. Työssä analysoitiin kaikki keskeiset valmistusvaiheet, kuten esivalmistelu, Braggin kuituhilan kirjoitusprosessi sekä jälkikäsitely ja kuituhilan karakterisointi. Valmistusprosessi osoittautui luotettavaksi, toistettavaksi ja se skaalattavissa monille eri kuitutyypeille eri sovelluskohteisiin. Valmistusprosessin optimointia ja luotettavuutta halutaan parantaa vielä, jotta sitä voidaan käyttää yksitaajuisten lasereiden sovellutuksia varten.

Lisäksi työssä arvioitiin Modulightilla valmistettujen suurihalkaisijoiden Braggin kuituhilojen soveltuvuutta lämpötilasensoreina. Tulokset osoittivat, että valmistetut kuituhilat saavuttivat tarvittavan suorituskyvyn, sillä niiden lämpötilamittauksen tarkkuus oli $\sigma_{T'} = 0.55^{\circ}\text{C}$, mikä on lähes sama kuin kaupallisen referenssisensorin tarkkuus 0.55°C . Tämä osoittaa, että valmistetut hilat voivat saavuttaa kaupallisten anturien tason ja tämän lisäksi mahdollistaa paremman mekaanisen kestävyuden.

Työn tuloksena kehitettiin systemaattinen ja luotettava Braggin kuituhilojen valmistusprosessi, joka on nyt otettu käyttöön Modulight Oyj:llä. Lisäksi suurihalkaisijoiden Braggin kuituhilat osoittivat potentiaalia tarkkuutta ja kuitujen kestävyyttä vaativissa mittaussovellutuksissa.

Avainsanat: optinen kuitu, Braggin kuituhila, fotosensitiivisyys, FBG-valmistus, FBG-ilmaisim

Tämän julkaisun alkuperäisyys on tarkastettu Turnitin OriginalityCheck -ohjelmalla.

PREFACE

This thesis was carried out at Modulight Corporation, and I am deeply grateful for the invaluable opportunities and experiences it has provided. I would like to extend my heartfelt thanks to my supervisor, D.Sc. (Tech) Regina Gumenyuk, for her expert guidance throughout this journey. I am equally indebted to my colleague and supervisor, Ph.D. and RD engineer Andrei Fedotov, for his unwavering support and deep knowledge of fiber lasers.

I am immensely thankful to Modulight Corporation for allowing me to grow and learn alongside the incredible laser family over these past years. A special note of gratitude for this goes to Seppo Orsila and Petteri Uusimaa for believing in me and giving me this opportunity. I also wish to express my appreciation to everyone at Modulight for fostering a positive and inspiring work environment, as well as for the countless meaningful conversations about work and life. Special thanks go to Kirsi Rantala for the countless meaningful conversations, advice, and laughs we have shared, as well as to Ville Vilokkinen, Dr. Lasse Orsila, and Andreas Schramm for sharing their expertise on lasers and providing invaluable guidance in shaping my career and personal growth.

The past seven years with my fellow Teekkaris have been profoundly enriching. I am deeply thankful to all my peer students at TUNI for sharing these years filled with physics labs, laskarit, pedagogical studies, and countless other shared experiences. I owe much of who I am today to Hiukkanen and my beloved Kyykkä companions, with whom I have shared so many unforgettable moments. A special thank-you goes to my friend Timo Hartikainen, with whom I have had the pleasure of creating countless cherished memories.

Finally, I wish to express my deepest gratitude to my family. To my mother, thank you for your unwavering support and guidance; to my father, for your wisdom and life lessons; to my twin brother, Jouni, for always being there with me through thick and thin—words cannot express how grateful I am for you. And to my dear Sanna, thank you for your constant motivation and encouragement to be the best version of myself.

In Tampere, 4th March 2025

Jesse Peltoniemi

CONTENTS

1.	Introduction	1
2.	Principles of Fiber Bragg gratings	3
2.1	Single-mode optical fiber	3
2.1.1	Light propagation	4
2.1.2	Fiber modes	6
2.2	Fiber Bragg Gratings	8
2.2.1	Uniform fiber Bragg gratings.	10
2.2.2	Chirped fiber Bragg gratings	12
2.3	Principles of FBG sensors	13
2.3.1	Bragg wavelength sensitivity	14
2.3.2	Fiber design for FBG sensors	16
3.	FBG fabrication methods	17
3.1	Photosensitivity	17
3.1.1	Germanium-doped silica fibers.	18
3.1.2	Hydrogenation and deuteration of the optical fiber	20
3.1.3	Thermal annealing of the optical fiber	22
3.2	FBG inscription	22
3.2.1	Phase mask inscription method	23
3.2.2	Interferometric inscription method	24
3.2.3	Point-by-point inscription method	26
4.	Development of FBG fabrication process	28
4.1	Deuteration of the optical fiber	28
4.2	FBG inscription	29
4.3	Thermal annealing of the FBG	31
4.4	Characterization of the FBG	33
4.4.1	Characterization setup	33
4.4.2	Analysis of the characterization data	34
5.	Implementation of FBG inscribed in a large diameter optical fiber as a temperature sensor	36
5.1	Methodology for FBG characterization	36
5.2	Analysis of commercial temperature sensor	36
5.2.1	Temperature sensitivity analysis	38
5.3	FBG-based temperature sensor in a large diameter optical fiber	39
5.3.1	Fabrication and characterization of FBG	40

5.3.2	FBG temperature sensitivity	41
5.3.3	FBG temperature sensitivity depending on the distance from the measurement point	47
6.	Conclusions	50
	References	52

LIST OF SYMBOLS AND ABBREVIATIONS

K_B	sensitivity
LP_{01}	fundamental mode
N	number density of oscillators of the medium
P_e	strain optic coefficient
R	reflectivity
T	temperature
V	V-number
V	normalized frequency parameter
X	measurand
Δn	amplitude modulation of the refractive index
Λ_g	grating period
Ω	coupling coefficient
α'	"physical length" change coefficient
α_f	thermal expansion coefficient
β	propagation constant
γ	phase shift
λ_B	Bragg wavelength
λ_{cutoff}	cutoff wavelength
μ_0	vacuum magnetic permeability
\overline{B}	magnetic flux vector
\overline{D}	electric flux density vector
\overline{E}	electric field vector
\overline{H}	magnetic field vector
\overline{J}	current density vector
\overline{M}	magnetic polarization
\overline{P}	electric polarization
ϕ	chirp of the grating

ρ	charge density
ρ	overall reflectivity
ρ_a	stress-optic coefficient
ρ_{11}	stress-optic tensor coefficient
σ	conductivity
σ_T	measurement accuracy in temperature
σ_λ	measurement accuracy in wavelength
σ_p	Poisson's ratio
σ_s	stress
$\sigma_{T'}$	measurement accuracy in temperature
ε_0	vacuum dielectric constant
\tilde{E}	Fourier transform of electric field vector
\tilde{E}_{clad}	electric field in the cladding of the optical fiber
\tilde{E}_{core}	electric field in the core of the optical fiber
\tilde{H}	Fourier transform of magnetic field vector
\tilde{H}_{clad}	electric field in the cladding of the optical fiber
\tilde{H}_{core}	electric field in the core of the optical fiber
\tilde{P}	Fourier transform of electric polarization vector
$\tilde{\chi}_{ij}$	Fourier transform of general second rank tensor for linear susceptibility
ζ	thermo-optic coefficient
a	core radius of optical fiber
b	normalized propagation constant
g	apodization
k	wavenumber
n	refractive index
n_0	average refractive index
n_{clad}	refractive index of the cladding
n_{core}	refractive index of the core
n_{eff}	effective refractive index
$n_{grating}$	refractive index of the grating
r	local reflectivity

CFBG	chirped fiber Bragg grating
CMT	coupled mode theory
CW	continuous wave
DBR	distributed Bragg reflector
FBG	fiber Bragg grating
FC/APC	ferrule connector/angled physical contact
NTC	negative temperature coefficient
OSA	Optical spectrum analyzer
PCB	printed circuit board
SLED	superluminescent diode
TEC	thermoelectric cooler
UFBG	uniform fiber Bragg grating
UV	ultraviolet

1. INTRODUCTION

The motivation for this work arises from the growing need for reliable and precise temperature monitoring systems across various industries. Temperature is a critical parameter in numerous applications, including industrial processes, environmental monitoring, health-care, and aerospace engineering. Traditional temperature sensing methods often face challenges such as slow response times, susceptibility to electromagnetic interference, and the necessity for frequent recalibration. In contrast, FBG-based temperature sensors are highly sensitive, immune to electromagnetic interference, compact, and capable of multiplexing, making them well-suited for modern sensing needs.

Fiber Bragg gratings (FBGs) are passive optical devices comprising periodic refractive index modulations inscribed in the core of an optical fiber over a finite length. These periodic variations result from a periodic perturbation in the photosensitivity of the fiber core, achieved through advanced fabrication techniques such as holographic inscription, phase mask methods, and point-by-point techniques. These precise fabrication processes enable tailoring the grating's properties to suit specific applications. The lightweight design, high resolution, and wide dynamic range of FBGs make them superior to conventional electrical sensors, which often struggle with issues like signal loss, electromagnetic interference, and safety in hazardous environments.

The unique sensing capabilities of FBGs arise from their ability to detect changes in external parameters—such as strain, temperature, pressure, and refractive index—by monitoring shifts in the Bragg wavelength. This sensitivity, combined with integrating multiple sensors along a single optical fiber, enables distributed sensing over large structures, making FBGs indispensable for precision-demanding applications like pipeline monitoring, wind turbine health assessments, aircraft stress analysis, and biomedical diagnostics.

This work is done in collaboration with Modulight Corporation, dedicated to the development and optimization of a fiber Bragg grating fabrication process. It emphasizes all stages of the FBG fabrication process: pre-inscription, the grating inscription mechanism, post-inscription processing, and characterization. Additionally, this work evaluated the properties of in-house inscribed large-diameter FBGs for temperature-sensing applications.

The thesis consists of 6 chapters. In Chapter 2, the fundamental physics and properties of

Fiber Bragg gratings are introduced coupled with the principles of FBG sensing. Chapter 3 deals with the photosensitivity and fabrication methods of FBGs. Chapter 4 covers the development of the FBG fabrication process. Chapter 5 focuses on the temperature sensing properties of larger-diameter FBG sensors. The final chapter 6 concludes this work.

2. PRINCIPLES OF FIBER BRAGG GRATINGS

Fiber Bragg grating is an optical element that is inscribed within the core of a single-mode optical fiber. The FBG induces periodic or aperiodic refractive index modulation, which reflects some of the light propagating in the fiber under certain conditions. The refractive index modulation properties can be influenced by external factors, such as temperature, which in turn changes the reflected properties of the light.

This chapter focuses on the propagation of light in the optical fiber, and the physics and properties of the fiber Bragg gratings. It concludes with the sensing principles of FBG-based sensors.

2.1 Single-mode optical fiber

A typical optical fiber consists of three components: a core made of doped silica glass, a cladding that surrounds the core, and an outer coating, which provides mechanical protection for the fiber. In addition, there might be an extra protective layer (strength member and outer jacket) for better mechanical protection [1]. The refractive index difference between the core and the cladding induces total internal reflection within the optical fiber, enabling the transmission of light through the fiber when the refractive index of the cladding is lower than that of the core.

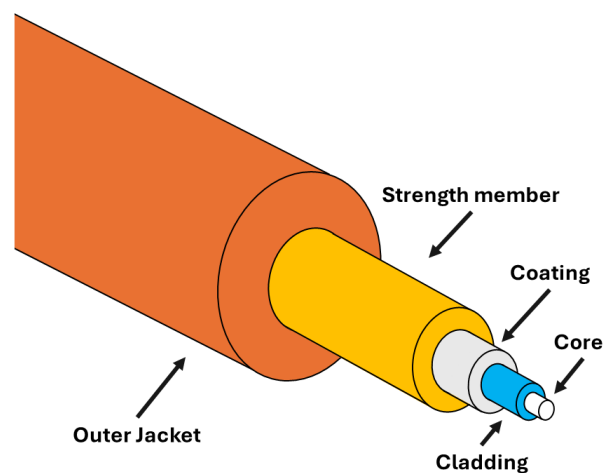


Figure 2.1. Structure of an optical fiber adapted from [1].

Optical fibers can display various refractive index profiles to incorporate the total internal reflection. Figure 2.2 illustrates two common refractive index profiles: step- and graded-index profiles.

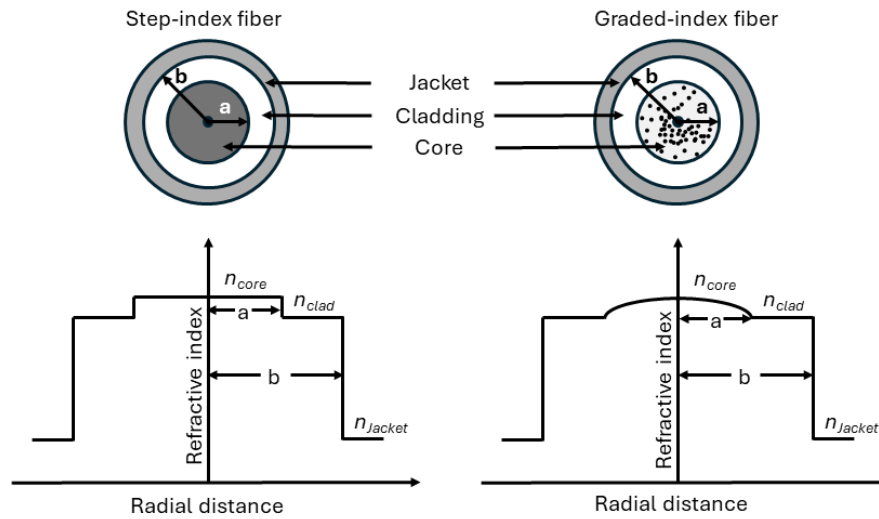


Figure 2.2. Cross section and refractive index profiles for step- and graded-indexed fibers adapted from [2].

In a step-index profile, the refractive index abruptly changes from the core to the cladding, resulting in a sharp transition. This configuration is characterized by a uniform refractive index within the core. Step-index profile fibers are characteristic of single-mode optical fibers.

Conversely, a graded-index profile features a gradual change in refractive index from the core to the cladding. This gradual variation results in a smoother transition of the optical properties, leading to improved performance in terms of dispersion and bandwidth. [3] Graded-index profiles are characteristic of multimode optical fibers.

2.1.1 Light propagation

This section discusses the properties of light propagating through the optical fiber and why single-mode fibers are commonly used for FBG inscription.

The propagation of electromagnetic waves is described with Maxwell's equations:

$$\begin{aligned}
 \nabla \cdot \bar{D} &= \rho \\
 \nabla \cdot \bar{B} &= 0 \\
 \nabla \times \bar{E} &= -\frac{\partial \bar{B}}{\partial t} \\
 \nabla \times \bar{H} &= \bar{J} + \frac{\partial \bar{D}}{\partial t},
 \end{aligned} \tag{2.1}$$

where \overline{D} is the electric flux density vector, ρ represents the charge density, \overline{B} signifies the magnetic flux vector, \overline{E} denotes the electric field vector, \overline{H} stands for the magnetic field vector, and \overline{J} describes the current density vector. The current density vector of such a medium is defined as, $\overline{J} = \sigma \overline{E}$, where σ is the conductivity of the medium. In the absence of charge density ($\rho = 0$) and negligible conductivity ($\sigma \approx 0$) in silica, a lossless medium is assumed.

In any medium the electric - and magnetic flux vectors are defined respectively:

$$\begin{aligned}\overline{D} &= \varepsilon_0 \overline{E} + \overline{P} \\ \overline{B} &= \mu_0 \overline{H} + \overline{M},\end{aligned}\tag{2.2}$$

where ε_0 is the dielectric constant in a vacuum, \overline{P} represents the electric polarization of the medium, μ_0 signifies the magnetic permeability in a vacuum, and \overline{M} denotes the magnetic polarization. Due to the nonmagnetic nature of silica, $\overline{M} = 0$ can be assumed.

Using these relations 2.2 and the curl of equations $\nabla \times \overline{E}$ and $\nabla \times \overline{H}$ the wave equation can be expressed as:

$$\nabla \times \nabla \times \overline{E} = -\mu_0 \varepsilon_0 \frac{\partial^2 \overline{E}}{\partial t^2} - \mu_0 \frac{\partial^2 \overline{P}}{\partial t^2}.\tag{2.3}$$

Solving the equation 2.3 for \overline{E} using Fourier transform yields:

$$\overline{E}(\vec{r}, t) = \frac{1}{2\pi} \int_{-\infty}^{\infty} \tilde{E}(\vec{r}, \omega) e^{(-i\omega t)} d\omega,\tag{2.4}$$

where \tilde{E} is the Fourier transform of \overline{E} . Alternatively this can be expressed in the frequency domain as:

$$\overline{E}(\vec{r}, t) = \mu_0 \varepsilon_0 \omega^2 \tilde{E} + \mu_0 \omega^2 \tilde{P}.\tag{2.5}$$

The polarization \tilde{P} can be expressed in terms of \tilde{E} as:

$$\tilde{P} = \varepsilon_0 \tilde{\chi}_{ij} \tilde{E},\tag{2.6}$$

where $\tilde{\chi}_{ij}$ represents the Fourier transform of the general second-rank tensor for linear susceptibility, related to the refractive index by $n(\omega)^2 = 1 + \tilde{\chi}(\omega)$.

With the identity:

$$\nabla \times \nabla \times \tilde{E} = \nabla(\nabla \cdot \tilde{E}) - \nabla^2 \tilde{E}, \quad (2.7)$$

and the assumption of a homogeneous medium:

$$0 = \nabla \cdot \tilde{D} = \varepsilon_0 \nabla \cdot (1 + \tilde{\chi}) \tilde{E} = \varepsilon_0 n^2 \nabla \cdot \tilde{E}, \quad (2.8)$$

the equation 2.5 can be written as:

$$\nabla^2 \tilde{E} + \frac{\omega^2 n^2(\omega)}{c^2} \tilde{E} = 0. \quad (2.9)$$

Following analogous steps, a wave equation for \tilde{H} can be derived:

$$\nabla^2 \tilde{H} + \frac{\omega^2 n^2(\omega)}{c^2} \tilde{H} = 0. \quad (2.10)$$

The wave equations 2.9 and 2.10 describe the electric and magnetic behavior of light as it propagates through the fiber core and cladding. [4, pp. 59–62, 765–767], [5, p. 121]

2.1.2 Fiber modes

The electric and magnetic field vectors in the core, \tilde{E}_{core} and \tilde{H}_{core} , as well as those in the cladding, \tilde{E}_{clad} and \tilde{H}_{clad} , must satisfy the wave equations 2.9 and 2.10, respectively. However, the solutions within the core and the cladding are not independent; they are interconnected by boundary conditions imposed on \tilde{E} and \tilde{H} at the core-cladding interface. Simply stated, any pair of solutions to these wave equations that meets these boundary conditions constitute a fiber mode.

Each fiber mode propagates at different speeds within the fiber, resulting in different propagation constants β . This parameter determines the velocity at which pulse energy travels through the fiber. The fiber modes propagate partially within the cladding and partially within the core, leading to propagation constants that satisfy $kn_{clad} < \beta < kn_{core}$, where k represents the wavenumber of the mode and n_{clad} and n_{core} represent the refractive indices for the cladding and core respectively.

Instead of focusing only on the propagation constant of a mode, the refractive index $n_{eff} = \beta/k = \frac{\beta\lambda}{2\pi}$ can alternatively be considered. This effective index lies between the refractive indices of the cladding and the core. To define the effective refractive index, the propagation constant β needs to be determined, which is done using the normalized propagation constant b :

$$b = \frac{\beta^2 - k^2 n_{clad}^2}{k^2 n_{core}^2 - n_{clad}^2} = \frac{n_{eff}^2 - n_{clad}^2}{n_{core}^2 - n_{clad}^2}. \quad (2.11)$$

The normalized propagation constant can be approximated with a relative error less than 0.2% by the equation:

$$b \approx \left(1.1428 - \frac{0.9960}{V} \right)^2, \quad (2.12)$$

where V represents the V-number, also known as the normalized frequency parameter. The V-number is an important property derived from the solutions of the wave equations 2.9 and 2.10:

$$V = \frac{2\pi}{\lambda} a \sqrt{n_{core}^2 - n_{clad}^2}, \quad (2.13)$$

where a is the core radius of the optical fiber.

The cutoff wavelength λ_{cutoff} of the optical fiber can be determined using the V-number, which defines the smallest wavelength when the optical fiber supports only a single mode. This mode is also called the fundamental LP_{01} mode. If $V < 2.405$, the optical fiber is considered to be a single-mode fiber. Given that the parameter V decreases with the radius a and is defined by $\Delta = (n_{core} - n_{clad})/n_{core}$, this leads to single-mode fibers having small radius and small differences in core-cladding refractive indexes (e.g. $a = 4 \mu m$ $\Delta = 0.003$).

The refractive effective index can be approximated from 2.11 and 2.12 to be:

$$n_{eff} \approx n_{clad} + \left(1.1428 - \frac{0.9960}{V} \right)^2 \Delta n. \quad (2.14)$$

The value of Δ is typically small, resulting in nearly equal refractive indices for the core and cladding of the fiber. As a result, light energy is not strictly confined to the fiber core; a significant portion can also propagate in the cladding. The light energy is divided among the various modes supported by the fiber. As previously mentioned, these modes travel at different speeds within the fiber. Consequently, the energy in a narrow pulse at the fiber's input will spread out by the time it reaches the output. Therefore, it is preferable to design the fiber to support only a single mode. [4, pp. 63–65]

2.2 Fiber Bragg Gratings

A fiber Bragg grating is a structure fabricated in the core of a single-mode optical fiber, characterized by refractive index perturbation along the fiber. The refractive index modulation of an FBG is illustrated in Figure 2.3. FBGs are often inscribed by exposing the photosensitive fiber to ultraviolet (UV) radiation [6, p. 1263]. The process of fabricating an FBG, also known as inscribing the FBG, is discussed more in detail in Chapter 3.

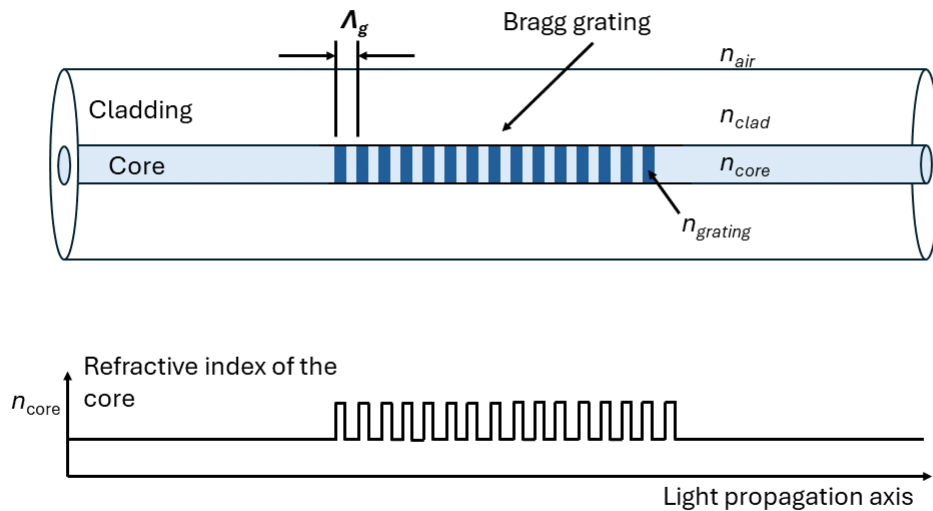


Figure 2.3. Illustration of fiber Bragg grating structure and refractive index modulation.

An FBG is one type of distributed Bragg reflector (DBR) that operates based on the principle of Fresnel reflections: when light encounters an interface between optically distinct materials with refractive indices n_{core} and $n_{grating}$, it undergoes partial reflection and transmission. Constructive interference occurs only at a specific wavelength λ_B across all interfaces. The reflectivity of the FBG is determined by the number of layer pairs and the refractive index contrast [7], [8].

Therefore, an FBG functions as a stop-band filter, reflecting a narrow band of incident light at the Bragg wavelength λ_B . Other wavelengths are out of phase and undergo destructive interference, transmitting through the material. The reflected wavelength λ_B is determined by:

$$\lambda_B = 2n_{eff}\Lambda_g, \quad (2.15)$$

where λ_B is the reflected wavelength from the FBG, n_{eff} is the effective refractive index,

and Λ_g is the period of the grating [6, p. 1267].

Coupled mode theory offers an explanation for the characteristics of FBG filters. The index perturbation $\delta n(z)$ is represented by a phase and amplitude-modulated periodic waveform:

$$\delta n(z) = \delta n_0(z) \left[1 + m \cdot \cos \left(\frac{2\pi z}{\Lambda_g} + \phi \right) \right]. \quad (2.16)$$

Here, n_0 is the average refractive index, and ϕ [9, p. 1277] represents the chirp of the grating. The envelope of the grating modulation and the average refractive index usually vary along the grating length. The clarity of the UV fringe pattern is shown by its contrast, which is determined by the parameter m [6, p. 1267].

The local reflectivity $r(z)$ within the FBG pattern describes the complex ratio between the amplitudes of forward and backward-going waves at a given point along the grating. This reflectivity is linked to the overall reflectivity ρ through a multiplicative phase factor of $e^{-i\gamma}$, where γ represents the phase shift induced by the grating. The relationship between the modified reflectivity $r(z)$ and the overall reflectivity ρ is governed by the following equation:

$$\rho' = i \left[\left(\frac{4\pi}{\lambda_B} \right) \left(\delta n_{eff} - \frac{\delta \lambda}{\lambda_B} - \phi' \right) \right] \rho + i\kappa (1 + \rho^2), \quad (2.17)$$

With a boundary condition of $\rho(L/2) = 0$, the coupling coefficient Ω is defined as:

$$\Omega = \left(\frac{\pi}{\lambda} \right) \delta n g(z) \eta, \quad (2.18)$$

where $g(z)$ represents the apodization function, typically Gaussian or raised-cosine weighting, and η denotes the modal overlap factor. Apodization modifies the reflectivity profile of an FBG by varying the refractive index along its length, represented by the function $g(z)$.

When the FBG has low reflectivity, Equation 2.17 can be linearized. Consequently, the reflectivity spectrum $\rho(-L/2, \delta \lambda)$ becomes proportional to the Fourier transform of $g(z)e^{-i\phi(z)}$. This relationship is a good way of choosing the suitable amplitude weighting for a given filter characteristic.

The reflectivity at the line center of the FBG ($\delta \lambda = 0$) is given by:

$$R = \rho\rho' = \tanh^2 [(\pi/\lambda) \delta n L \bar{g} \eta], \quad (2.19)$$

when δn_{eff} is neglected and \bar{g} represents the average value of the envelope function. This model accurately predicts the reflectivity and the FBG spectrum.

A feature that is observed in strongly reflected gratings (large index perturbations) is the formation of small sharp spectral resonances on the shorter side of the FBG line center. It forms due to the self-chirping from δn_{eff} . This leads to FBG to couple dissimilar modes in reflection and transmission provided that phases are synchronized and there is sufficient overlap with the modes. The phase matching condition is given as:

$$n_{eff} - \frac{\lambda}{\Lambda_z} = n'_{eff}, \quad (2.20)$$

where n_{eff} is the effective refractive index of the incident wave and n'_{eff} represents the effective refractive index of the grating-coupled wave. n'_{eff} is a negative quantity and the grating coupled wave can be either reflected or transmitted wave.

Propagation confined within ordinary bounds occurs when the wave's effective index falls between the core and cladding index values within the grating satisfying the Bragg condition 2.15. If the effective index remains below the cladding index n_{clad} , cladding modes are not excited in a single-mode fiber. Conversely, when the effective index exceeds the cladding index, multiple transmission dips emerge in the spectrum at shorter wavelengths than the Bragg wavelength. [6, pp. 1267–1269]

2.2.1 Uniform fiber Bragg gratings

Uniform fiber Bragg gratings (UFBG) are the simplest form of fiber Bragg Gratings, characterized by periodic refractive index modulation. The refractive index profile, as estimated by Equation 2.16, satisfies the Bragg condition outlined in Equation 2.15.

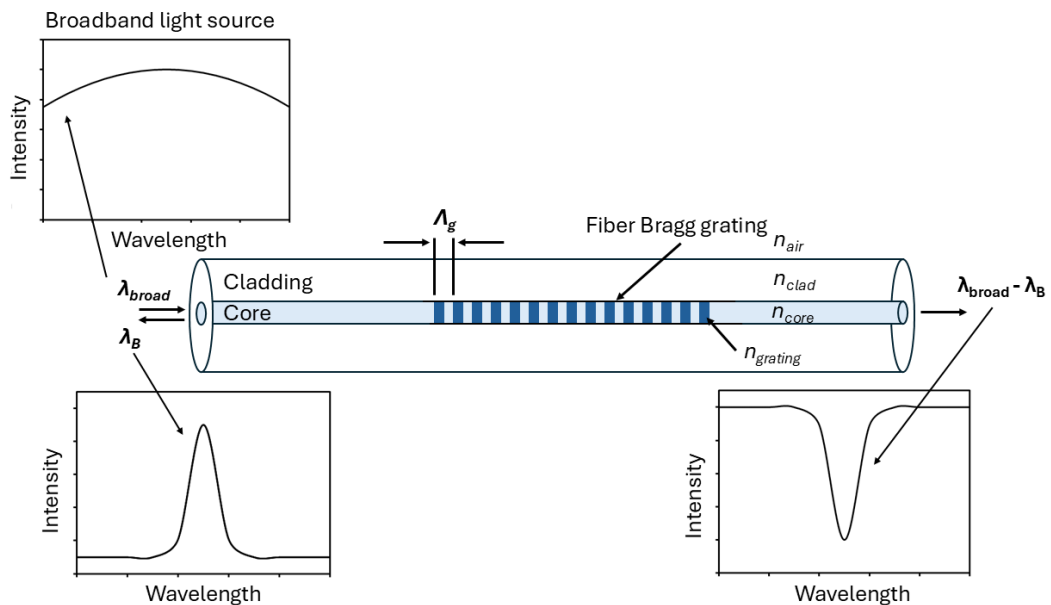


Figure 2.4. Illustration of a uniform fiber Bragg grating adapted from [10, p. 4322].

The modulation of the refractive index for uniform grating can be simplified from equation 2.16 to be:

$$n(x) = n_{eff} + \Delta n \cos\left(\frac{2\pi x}{\Lambda_g}\right), \quad (2.21)$$

where Δn represents the amplitude modulation of the refractive index which is typically around $10^{-5} - 10^{-2}$. Λ_g is the grating period, and x denotes the distance along the longitudinal axis of the fiber.

Utilizing coupled-mode theory, the reflectivity spectrum $R(L, \lambda)$ of the grating can be expressed as:

$$R(L, \lambda) = \frac{\Omega^2 \sinh^2(sL)}{\Delta\beta^2 \sinh^2(sL) + s^2 \cosh^2(sL)}, \quad (2.22)$$

where Ω is the coupling coefficient, $\Delta\beta = \beta - \pi/\Lambda_g$ [11, p. 3] represents the detuning vector and $\beta = 2\pi n_{eff}/\lambda$ signifies the propagation constant. Parameter s^2 can be expressed as $s^2 = \Omega^2 - \Delta\beta^2$ which is either real or imaginary: $s = \sqrt{\Omega^2 - \Delta\beta^2}$ if $\Omega^2 > \Delta\beta^2$ or $s = i\sqrt{\Delta\beta^2 - \Omega^2}$ if $\Omega^2 < \Delta\beta^2$ [12, p. 22].

The coupling coefficient for the sinusoidal variation of index perturbation along the fiber axis is given by:

$$\Omega = \frac{\pi \Delta n \eta(V)}{\lambda} \quad (2.23)$$

where $\eta(V) \approx 1 - 1/V^2$ with V representing the V -number of the fiber.

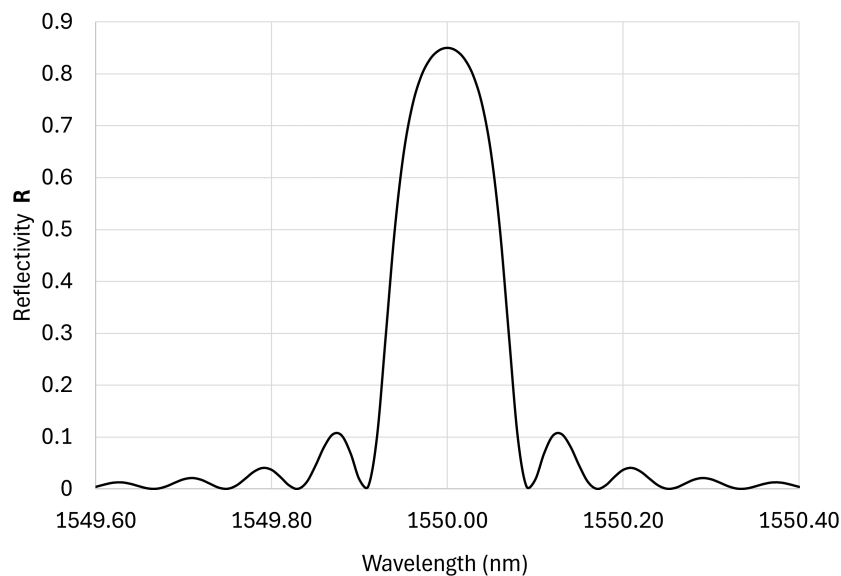


Figure 2.5. Calculated uniform fiber Bragg grating reflection spectrum.

Figure 2.5 shows the calculated reflection spectrum of the Fiber Bragg grating, which is computed with the following values: $n_{eff} = 1.48$, $\Delta n = 10^{-4}$, $V = 2.19$ Λ_g matching $\lambda_B = 1550 \text{ nm}$. The calculated reflection spectrum of FBG shows a reflection peak at the Bragg wavelength of $\lambda_B = 1550 \text{ nm}$. [10, p. 4323]. The main peak is flanked by side lobes, which result from finite grating length. These side lobes represent weaker reflections at wavelengths near the Bragg wavelength and are typically minimized in optimized grating designs to reduce signal interference.

2.2.2 Chirped fiber Bragg gratings

In contrast to uniform gratings, chirped fiber Bragg gratings (CFBGs) have an aperiodic refractive index modulation. While the grating period Λ_g remains constant in uniform gratings, in CFBGs, the grating period function $\Lambda_g(z)$ defines the chirp pattern, which is typically linear along the grating. Figure 2.6 a) illustrates linear chirp along the grating period (linearly increasing grating period) and b) shows that each of these different grating periods can be thought of as subsequent uniform FBGs.

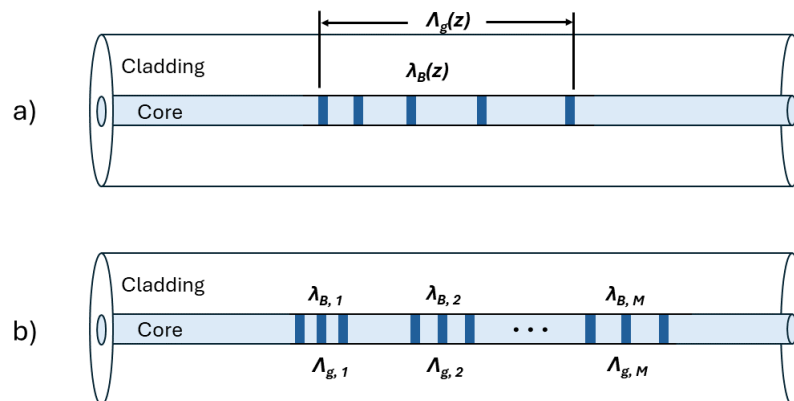


Figure 2.6. Schematic of chirped fiber Bragg grating (a) and the discretization method of chain of M number of uniform gratings (b). Adapted from [13, pp. 2147, 3].

The introduction of chirp implies that each section of the grating reflects at a different Bragg wavelength, thereby widening the overall spectrum compared to the uniform grating. Chirped fiber Bragg gratings can be thought of as consisting of multiple (M) subsequent uniform FBGs, each having a unique Bragg wavelength λ_B . The total reflectivity (R) could be calculated using Erdogan's coupled-mode theory (CMT), but this analysis is beyond the scope of this study.

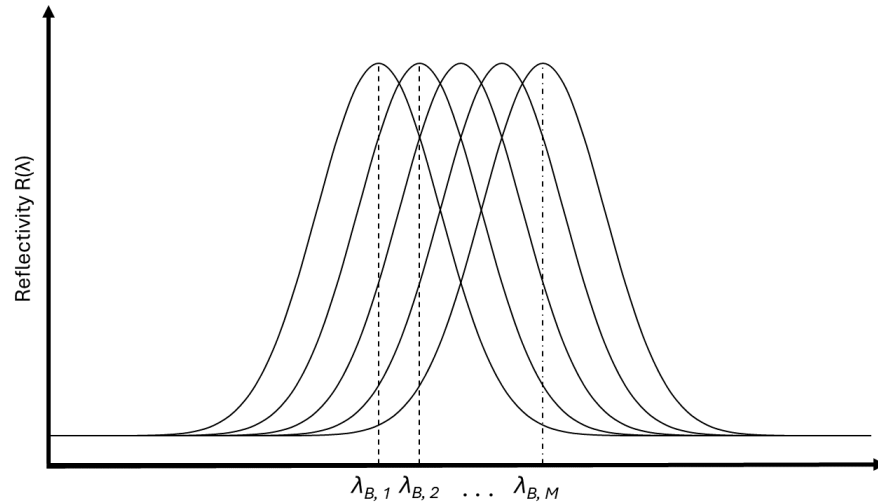


Figure 2.7. Schematic of CFBG and its incoherent discretization method. Adapted from [13, pp. 2147, 3].

CFBGs have distinct characteristics that differentiate them from uniform FBG arrays. While uniform FBG arrays typically have lengths up to 5 mm, with a minimum distance between sensing elements of around 10 mm, CFBGs exhibit longer lengths ranging typically from 15 to 50 mm. In addition, CFBGs can perform short-length distributed sensing, allowing them to detect precise, spatially resolved variations in temperature or strain with high resolution—down to the millimeter scale along the grating’s length. [13, pp. 2147, 1–3]

2.3 Principles of FBG sensors

Fiber Bragg gratings are highly sensitive optical devices that respond to changes in their surrounding environment. Factors such as temperature, strain, vibration, and pressure affect the material properties of the glass, which in turn influence the refractive index of the core and the overall waveguide behavior. While FBGs are capable of detecting a wide range of parameters, accurately distinguishing between them requires careful analysis. With unique Bragg wavelengths, FBGs can be cascaded along a single fiber for multiplexed sensing, as long as their signals remain distinct and non-overlapping. [14]

The FBGs are commonly used for temperature and strain sensing. In these applications, the changes in the refractive index of the optical fiber core are both temperature and strain-dependent. This can be expressed as:

$$\partial n_{eff} = \frac{\partial n_{eff}}{\partial T} \Delta T + \frac{\partial n_{eff}}{\partial \sigma_s} \Delta \sigma_s, \quad (2.24)$$

where $\partial n/\partial T$ is the temperature coefficient of the refractive index, ΔT is the temperature change in the fiber, $\partial n/\partial \sigma$ is the longitudinal stress optic coefficient, and $\Delta \sigma_s$ is the

applied stress along the optical fiber. [5, pp. 81-82]

2.3.1 Bragg wavelength sensitivity

As shown in Equation 2.15, the reflected Bragg wavelength depends on the effective refractive index of the core as well as on the periodicity of the grating. By measuring the changes in the Bragg wavelength, an external parameter X can be monitored. The external parameter could be one of the parameters mentioned at the beginning of Section 2.3, which could be temperature T , strain, ε , hydrostatic pressure, P_h , or refractive index of the cladding, n_{clad} . The change in Bragg wavelength can be calculated as:

$$\begin{aligned}\lambda_B &= 2n_{eff}\Lambda_g, \\ \frac{\partial\lambda_B}{\partial X} &= 2\frac{\partial}{\partial X}(n_{eff}\Lambda_g) = 2\Lambda_g\frac{\partial n_{eff}}{\partial X} + 2n_{eff}\frac{\partial\Lambda_g}{\partial X}, \\ &= 2\Lambda_g\delta n_{eff} + 2n_{eff}\Lambda_g\alpha', \\ \frac{1}{\lambda_B}\frac{\partial\lambda_B}{\partial X} &= \frac{2\Lambda_g\delta n_{eff}}{2n_{eff}\Lambda_g} + \frac{2n_{eff}\Lambda_g\alpha'}{2n_{eff}\Lambda_g} = \frac{\delta n_{eff}}{n_{eff}} + \alpha',\end{aligned}\tag{2.25}$$

where $\delta n_{eff}/n_{eff}$ is the normalized sensitivity of the effective index of the mode and α' is the coefficient of the "physical length" change. Now the Bragg wavelength change can be written as using the 2.25:

$$\begin{aligned}\Delta\lambda_B &= \frac{\partial\lambda_B}{\partial X}\Delta X = \lambda_B\left(\frac{1}{n_{eff}}\delta n_{eff} + \alpha'\right)\Delta X, \\ &= \lambda_B\left(\frac{1}{n_{eff}}\frac{\partial n_{eff}}{\partial X} + \frac{1}{\Lambda}\frac{\partial\Lambda}{\partial X}\right)\Delta X.\end{aligned}\tag{2.26}$$

[5, p. 444]

Now the sensitivity of the FBG $K_{B,X}$ to a specific parameter X can be defined as [15, p. 75]:

$$K_{B,X} = \frac{\Delta\lambda_B}{\Delta X} = \lambda_B\left(\frac{1}{n_{eff}}\frac{\partial n_{eff}}{\partial X} + \frac{1}{\Lambda}\frac{\partial\Lambda}{\partial X}\right).\tag{2.27}$$

The sensitivity $K_{B,X}$ defined in Equation 2.27 characterizes the responsiveness of the FBG sensor to variations in the external parameter X . It quantifies how much the reflected Bragg wavelength (λ_B) changes with respect to a unit change in X .

Temperature sensors

With Equation 2.26, it is possible to determine the effect of temperature on the Bragg wavelength. The temperature dependence can be derived as:

$$\begin{aligned}\Delta\lambda_B &= \lambda_B \left(\frac{1}{n_{eff}} \frac{\partial n_{eff}}{\partial T} + \frac{1}{\Lambda} \frac{\partial \Lambda}{\partial T} \right) \Delta T \\ &= \lambda_B (\zeta + \alpha_f) \Delta T,\end{aligned}\quad (2.28)$$

where the ζ is the thermo-optic coefficient $\partial n/\partial T$ and α_f is the thermal expansion coefficient. [15, p. 75] From literature, the following values are true for a Silica fiber: The thermo-optical coefficient is $1.090 \times 10^{-5}/^\circ\text{C}$, the thermal expansion coefficient is $0.55 \times 10^{-6}/^\circ\text{C}$ and the effective refractive index is 1.448 [16, pp. 5881–5882], [17, p. 1]. Based on the application the Bragg wavelength of the FBG can be tailored. Bragg wavelength of 1550 nm is commonly used. The sensitivity of such an FBG can be calculated using Equation 2.28 which yields for sensitivity of $K_{B,T} = 11.8 \text{ pm}/^\circ\text{C}$.

Strain sensors

The application of fiber Bragg grating (FBG) sensors extends beyond just temperature sensing; another common and significant application lies in strain measurement. By exploiting the inherent sensitivity of FBG sensors to mechanical deformations, they serve as robust and precise tools for monitoring structural strain.

The same procedures can be applied to calculate the strain as well. Equation (2.29) describes the change in Bragg wavelength due to strain along the optical fiber:

$$\Lambda_B = \lambda_B(1 - \rho_a)\varepsilon_s, \quad (2.29)$$

where ρ_a is the the stress-optic coefficient:

$$\rho_a = \frac{n_{eff}^2}{2} [\rho_{12} - \sigma_p (\rho_{11} - \rho_{12})]. \quad (2.30)$$

Here, ρ_{11} and ρ_{12} are coefficients of the stress-optic tensor, and σ_p represents the Poisson's ratio.

For isotropic and homogeneous strain, Equation (2.31) can be used:

$$\Delta\lambda_B = \lambda_B (1 - P_e) \varepsilon_s. \quad (2.31)$$

where P_e is the strain-optic coefficient. [5, p. 444]

2.3.2 Fiber design for FBG sensors

In sensing with an optical fiber Bragg grating, the variation of the Bragg wavelength depends on the measurand. External factors like temperature or pressure can significantly impact this wavelength change. It's important to note that the optical mode within the fiber isn't solely confined to the core; rather, it extends into the cladding as well. Temperature affects both the core and cladding's refractive indices and the fiber's length. Consequently, there's a change in the effective index of the mode in two main ways. Firstly, even if both the core and cladding refractive indices change equally, the propagation constant of the mode changes proportionally. Secondly, a differential change in refractive index between the core and cladding materials affects the propagation constant. Considering the effective mode index, denoted as n_{eff} , it is influenced by these factors. Remembering the effective refractive index from the equation 2.14 to be:

$$n_{eff} \approx n_{clad} + \left(1.1428 - \frac{0.996}{V}\right)^2 \Delta n. \quad (2.32)$$

The alteration in the effective index arises from variations in the V-value of the fiber concerning a specific core-cladding refractive index difference. Upon differentiating Equation 2.32, the condition for the change in the mode effective index n_{eff} in terms of the v-value ($1.5 < V < 2.5$) is expressed as follows:

$$\frac{\partial n_{eff}}{\partial v} \approx \left(\frac{1.23}{V^2} - \frac{1.98}{V^3}\right) \Delta n. \quad (2.33)$$

From this, it can be determined that the value of n_{eff} exhibits the highest sensitivity at a V-value of approximately 1.3.

Since the V-value depends on the core-cladding refractive index difference, any disparity in their refractive indices will have the greatest impact on the mode's effective index. Given the usual differences between the core and cladding, external factors like temperature changes affect the v-value. Thus, operating under these conditions makes the fiber highly sensitive to temperature measurements, primarily due to effective refractive index changes.

Typically, the impact of the differential refractive index is relatively small, becoming notable only with substantial temperature changes from tens to hundreds of degrees Celsius. [5, pp. 445–446]

3. FBG FABRICATION METHODS

The phenomenon where exposure to ultraviolet light permanently changes the refractive index is known as photosensitivity. Most fiber types can exhibit photosensitivity dependent on various photomechanical and thermochemical mechanisms. The contribution of these mechanisms depends on the fiber type, radiation intensity, and inscription wavelength. Although the precise mechanisms of photosensitivity are not fully understood, many theories explain the phenomenon, such as the Kramers-Kronig, dipole, and compaction models. These theories are commonly used to explain the photosensitivity of optical fiber. [18, p. 12]

FBG fabrication involves three primary phases: the pre-process, where the optical fiber is prepared to enhance its photosensitivity; the inscription process, during which the FBG structure is inscribed; and the post-process, aimed at stabilizing the fiber's refractive index and eliminating excess photosensitivity. Each process phase can be carried out using different methods, varying in complexity and suitability for specific applications.

This chapter introduces the most common methods for FBG fabrication, emphasizing those employed in this work.

3.1 Photosensitivity

Photosensitivity is characterized by a permanent alteration in the refractive index of a medium occurring due to the modification of chemical or physical properties upon exposure to light. Various parameters such as the FBG fabrication process, fiber composition, and the fabrication light source (operational wavelength and operation type (pulsed vs continuous wave)) significantly influence the photosensitivity properties of optical fibers. [19, p. 279] Enhanced photosensitivity contributes to greater changes in altering the refractive index.

The refractive index of isotropic dielectric materials, such as silicate glass (used in optical fibers), can be represented mathematically by a summation of i oscillators, following a model such as:

$$\frac{n^2 - 1}{n^2 + 2} = \frac{4\pi N e^2}{3 m} \sum_i \frac{f_i}{\omega_i^2 - \omega^2 - i\Gamma_i \omega}, \quad (3.1)$$

where e and m represent the charge and mass of the electron respectively, n is the refractive index, N is the number density of oscillators atoms or molecules of the medium, f_i stands for the oscillator strength associated with the transition frequency ω_i , while Γ_i denotes the damping constant of the i^{th} oscillator. [20, pp. 234508–2]

From this equation, it is clear that the refractive index has both real and imaginary components. The real part affects the phase velocity of light and influences the propagation constant, while the imaginary part represents either loss or gain, depending on its sign [5, p. 6].

Losses can be introduced into the optical fiber when UV light gets absorbed. This absorption alters the refractive index at the absorption points. These changes in the refractive index occur at particular wavelengths, λ , which can be identified using the absorption spectrum in the ultraviolet region and applying the Kramers-Kronig relations:

$$\Delta n(\lambda) = \frac{1}{(2\pi)^2} \sum_i \int_{\lambda_2}^{\lambda_1} \frac{(\Delta\alpha_i(\lambda') \cdot \lambda'^2)}{(\lambda^2 - \lambda'^2)} d\lambda'. \quad (3.2)$$

The summation covers discrete wavelength intervals around each of the i changes in measured absorption α_i . Therefore, any photo-induced change in absorption within the range $\lambda_1 \leq \lambda' \leq \lambda_2$ will cause a change in the refractive index at wavelength λ [5, p. 8].

The quest for photosensitivity in optical fibers follows two main paths, each with its distinct approach. Firstly, photosensitivity can be built into the optical fiber during its manufacturing process, integrating the desired properties directly into the fiber's structure. Alternatively, post-processing techniques offer another route, allowing photosensitization to occur after the fiber has been made, providing more flexibility in modifying existing fibers.

These methods employ various techniques to achieve photosensitivity. For example, during manufacturing, boron, and tin can be added as codopants in germanosilicate fibers. On the other hand, post-processing methods include hot hydrogenation, cold high-pressure hydrogenation, and flame-assisted low-pressure hydrogenation. Each of these techniques plays a unique role in enhancing photosensitivity within optical fibers, promising advancements across a range of applications. [5, p. 21]

3.1.1 Germanium-doped silica fibers

Germanium-doped silica has germanium oxide (GeO) defects within the optical fiber. Germanium-doped fibers are made by collapsing the fiber in a reducing atmosphere, for

example, replacing oxygen (O) with nitrogen (N) or helium (He). In these fibers, the germanium atom is typically coordinated with either another germanium (Ge) or silicon (Si) atom, forming a bond that exhibits a characteristic absorption peak at approximately 240 nm. This absorption peak is a notable feature observed in photosensitive germanium-doped optical fibers.

Under ultraviolet illumination, this bond is susceptible to breakage, resulting in the formation of a GeE' center. Consequently, the electron from this center becomes mobile within the glass matrix. It is speculated that the removal of this electron leads to a reconfiguration of the molecule's shape, consequently altering the absorption characteristics of the molecule and potentially impacting the material's density. [5, p. 19-20, 22]

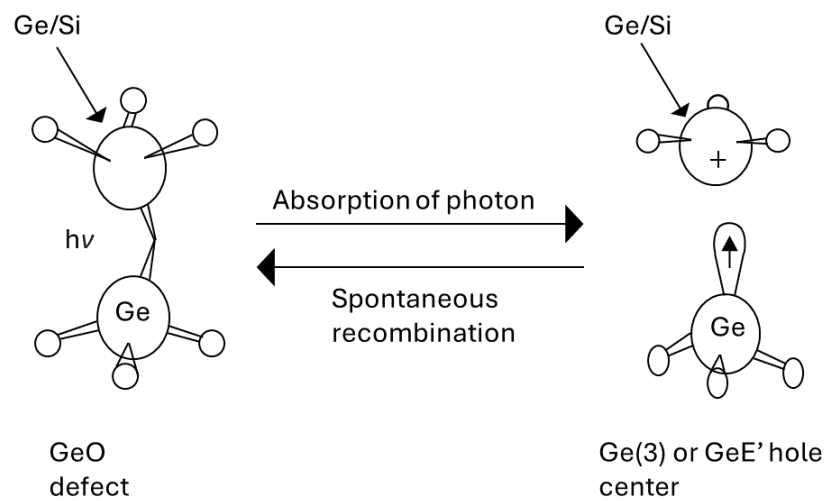


Figure 3.1. Breakage of GeO - Si/Ge bonds due to UV illumination adapted from [5, p. 20].

The variation in GeE' concentration centers results in changes in the UV absorption spectra, consequently leading to a direct alteration in the refractive index through Kramers-Kronig relations 3.2 [5, p. 36]. When germanium acts as a core dopant in silicate fiber, it forms suboxides such as GeO_x (with x ranging from 1 to 2), generating a spectrum of defects within the silica host glass. [5, p. 18]

There exists considerable interest in quantifying the concentration of GeO defects in the core, as it correlates closely with intrinsic photosensitivity [5, p. 22]. This concentration (C) can be directly linked to the absorption at 242 nm ($\alpha_{242\text{ nm}}$) through the relationship expressed as $k = \alpha_{242\text{ nm}}/C$, where k represents the molar absorption coefficient. Additionally, the distinctive absorption spectra for $Ge(1)$ and $Ge(2)$ are observed at approximately 280 nm and 213 nm respectively. These absorption peaks signify trapped electrons at Ge (or Si) sites and hole centers respectively [5, p. 19].

The refractive index change in standard fibers has an almost linear increase with the concentration of germanium (Ge) after exposure to UV radiation, ranging from approximately

3×10^{-5} to 2.5×10^{-4} for GeO_2 concentrations of 3 mol% and 20 mol% respectively. These results were obtained using continuous wave (CW) lasers. However, when employing a high-intensity ArF excimer laser with 50 pulses/s and a fluence of 50 mJ/cm^2 , for high-germania-doped fibers (8 %), the growth in refractive index can be significantly higher, reaching approximately 0.001. This considerable increase is due to two-photon absorption occurring at 193 nm. [21, p. 3529][5, p. 22]

High-germania-doped (10 – 30 mol%) fibers demonstrate low photosensitivity, with a refractive index change of approximately $\delta n \sim 1 \times 10^{-4}$ [5, p. 40].

Germanium-Boron codoped optical fibers

The addition of boron to germanosilicate fibers reduces the refractive index, enabling a higher concentration of germania to be incorporated into the core. For this reason, boron is typically used to dope the cladding, as the core requires a higher refractive index. By codoping with germanium and boron, a greater proportion of germanium can be utilized, increasing photosensitivity while maintaining a minimal refractive index difference [5, pp. 26–27].

This composition offers the advantage of producing fiber with a refractive index profile and core-to-cladding refractive index difference nearly identical to standard single-mode optical fibers, yet containing significantly more germania in the core [5, p. 27]. Boron-germanium-codoped fibers have demonstrated improved photosensitivity compared to germanium-doped fibers alone, achieving a refractive index change of approximately $\delta n \sim 1 \times 10^{-3}$ [5, pp. 37, 40].

3.1.2 Hydrogenation and deuteration of the optical fiber

Introducing an optical fiber to molecular hydrogen (H_2) can introduce new losses for the fiber, as noted in studies such as [22] and [23]. These losses may arise from unreacted hydrogen (H_2) or chemical reactions occurring within the fiber. For instance, reactions such as hydrogen combining with oxygen to form hydroxyl ions (OH^-), or the interaction of hydrogen with germanium in germanium-doped fibers to form GeH , can lead to loss mechanisms [5, p. 29].

The formation of GeH is significant, because it alters the band structure in the UV region, thereby influencing the refractive index according to the Kramers-Kronig model (see Equation 3.2). Similarly, the formation of OH-species upon UV exposure increases losses in the 1500-nm region, with wavelengths of $1.39 \mu\text{m}$ for Si-OH and $1.42 \mu\text{m}$ for Ge-OH. For instance, a concentration of 1 mol% of hydroxyl species can elevate the loss at $1.4 \mu\text{m}$ by approximately 5 dB. To mitigate these losses, exposing the fiber to deuterium instead of hydrogen shifts the first overtone OD of the water peak to approximately

1.9 μm [5, p. 31].

During the hydrogenation process, the fiber undergoes a "loading" mechanism wherein hydrogen molecules diffuse into its structure. It's worth noting that the extent of this loading process is influenced by temperature and pressure conditions. [5, p. 31].

The diffusion of molecular hydrogen can be mathematically described by the diffusion equation:

$$\frac{\partial C}{\partial t} - D\nabla^2 C = 0, \quad (3.3)$$

where C is the hydrogen concentration and D represents the diffusion coefficient [24, p. 936]. The diffusion coefficient D_{H_2} for hydrogen is determined by the expression

$$D_{H_2} = 2.83 \times 10^{-4} \exp\left(\frac{-40.19 \text{ kJ/mol}}{RT}\right) \text{ cm}^2/\text{s}, \quad (3.4)$$

where $R = 8.311 \text{ J/(K}\cdot\text{mol)}$ and the temperature T is expressed in Kelvins [23, p. 781]. The hydrogenation time required for the hydrogen concentration to reach 95 % can be approximated using

$$t_{0.95} = \frac{0.6a^2}{D_{H_2}}, \quad (3.5)$$

where a is the fiber radius [23, p. 781]. For instance, considering a fiber with a radius of 125 μm at a temperature of 25°C, this equation predicts an approximate hydrogenation time of around 42 days. Notably, both Equation 3.5 and Equation 3.4 do not explicitly account for pressure dependence, despite the recognized role of pressure during hydrogenation. It's worth mentioning that the magnitude of losses due to H_2 increases linearly with pressure, suggesting a linear relationship between hydrogen concentration and pressure P_{H_2} [23, p. 781]. For instance, hydrogenating a 125 μm diameter fiber at room temperature and 200 bar pressure for approximately 2 weeks is deemed sufficient [5, p. 29].

High-pressure cold hydrogen-soaked germania-doped fibers can achieve significantly improved photosensitivities, reaching values of $\delta n \sim 1 \times 10^{-2}$, which is at least ten times stronger than those observed in germanium-boron codoped optical fibers. This method is extremely versatile and enables easy fabrication since multiple different fiber types can be used including standard telecommunication fibers.

All of the above is true also for deuterium which can be used in place of hydrogen for the loading process. One benefit of using deuterium is that it does not cause losses at the 1300/1500 nm wavelengths, unlike hydrogen. This is because the OD (OH) overtones do

not overlap with the second or third telecommunications windows, avoiding those losses. However, the drawback is that deuterium is significantly more expensive [5, p. 40].

To prevent premature out-diffusion of the hydrogen or deuterium from the optical fiber, it should be stored at low temperatures, around $-70\text{ }^{\circ}\text{C}$, to inhibit the out-diffusion of deuterium from the optical fiber [5, p. 33]. This storage condition helps to maintain the enhanced photosensitivity properties for longer periods.

3.1.3 Thermal annealing of the optical fiber

Experimental findings demonstrate that the Bragg Wavelength λ_B shifts during the out-diffusion of hydrogen or deuterium, also known as annealing if it is carried at high temperature. As it diffuses out of the fiber, the Bragg wavelength decreases. The outward diffusion in cylindrical geometry can be described by the equation:

$$\frac{C}{C_0} = 1 - \exp\left(-\frac{a^2}{4Dt}\right), \quad (3.6)$$

where t is the time after the onset diffusion from a loaded sample. Experimental data shows that the time required to get rid of 95 % of e.g the hydrogen is estimated as:

$$t(h) = 2.063 \times 10^{-4} \exp\left(\frac{4079}{T(K)}\right). \quad (3.7)$$

This time can be regarded as the total annealing time. For instance, at room temperature ($20\text{ }^{\circ}\text{C}$), the annealing time would be nearly 10 days. However, increasing the temperature to $70\text{ }^{\circ}\text{C}$ would reduce the annealing time to around 30 hours [24, pp. 936–939].

3.2 FBG inscription

Hill Gratings, also known as internally written Bragg gratings, operate near the inscription wavelength, and it was the first grating inscription method discovered [25, p. 1187]. Operation at other wavelengths requires fabrication techniques that fall into two categories: holographic [26] and non-interferometric. Holographic techniques are based on the interference of the UV light source with the fiber, while non-interferometric techniques depend on the periodic exposure of the fiber to pulsed sources or through a spatially periodic amplitude mask. Despite different methodologies, both these techniques form the fiber Bragg grating through the side of the cladding. [5, p. 53] The phase mask inscription method and interferometric inscription methods are examples of the holographic inscription method, and point-by-point inscription is an example of the non-interferometric inscription method.

3.2.1 Phase mask inscription method

The use of phase masks in the interferometer setup has been a significant advancement in simplifying the process of FBG inscription. In this method, the grating is inscribed from the side of the fiber. The operational principle relies on the diffraction of incoming UV radiation into several orders, which are denoted as $m = 0, \pm 1, \pm 2$, and so on. This process is illustrated schematically in Figure 3.2. Both the incoming and diffracted orders fulfill the general diffraction equation, where the period Λ_{pm} of the phase mask is:

$$\Lambda_{pm} = \frac{m\lambda_{uv}}{\sin(\theta_m/2) - \sin(\theta_i)}, \quad (3.8)$$

where $\theta_m/2$ is the angle of the diffracted order, λ_{uv} stands for the UV wavelength, and θ_i denotes the angle of the incident UV beam. When the period of the grating falls between λ_{uv} and $\lambda_{uv}/2$, the incident wave undergoes diffraction into a sole order ($m = -1$), while the remaining power persists in the transmitted wave ($m = 0$).

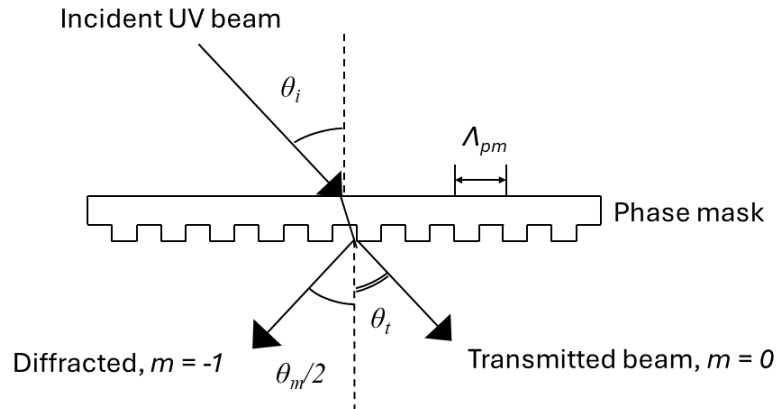


Figure 3.2. A schematic of the diffraction of an incident beam coupled at the angle from a phase mask adapted from [5, p. 56].

When UV radiation is incident at a normal angle $\theta_i = 0$, the diffracted radiation divides into $m = 0$ and ± 1 orders, as illustrated in figure 3.3. The interference pattern formed at the fiber, where two such beams of order 1 converge due to parallel mirrors, exhibits a period Λ_g that correlates with the diffraction angle $\theta_m/2$ by

$$\Lambda_g = \frac{\lambda_{uv}}{2\sin(\theta_m/2)} = \frac{\Lambda_{pm}}{2}. \quad (3.9)$$

The period Λ_{pm} of the grating etched in the mask is determined by the Bragg wavelength λ_B required for the grating in the fiber and utilizing 3.9 to derive

$$\Lambda_g = \frac{N\lambda_B}{2n_{eff}} = \frac{\Lambda_{pm}}{2}, \quad (3.10)$$

where $N \geq 1$ is an integer indicating the order of the grating period. [5, pp. 55–56]

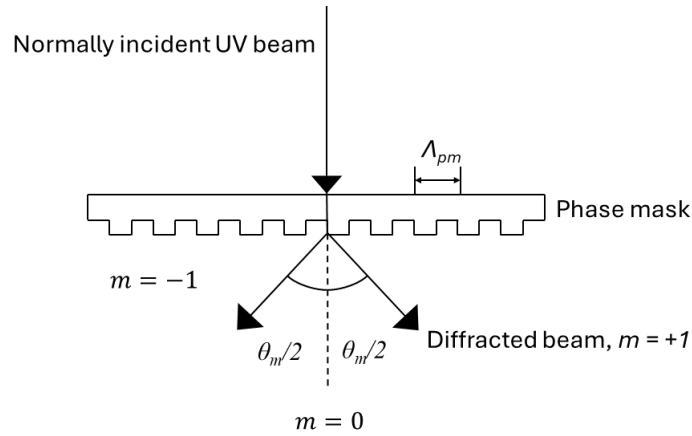


Figure 3.3. Schematic of normally incident UV beam diffracted into first-orders. Adapted from [5, p. 56]

In summary, the UV wavelength, phase mask period, and grating period are interdependent. Since the UV light source is fixed, the desired Bragg wavelength for manufacturing FBGs dictates the required phase mask period. Together, these factors determine the specifications for the phase mask to achieve the desired results. Because the grating period will be fixed based on the phase mask design, it makes this inscription technique limited for making only one kind of gratings. However, this enables the mass production of identical FBGs compared to other inscription techniques.

3.2.2 Interferometric inscription method

The formation of the fiber Bragg grating through the side of the cladding in a bulk interferometer is illustrated in Figure 3.4. The interferometer's working principle is that the UV beam is split into two equal powers at the beam splitter. The beam is then guided into the side of the optical fiber at a mutual angle of θ from two UV mirrors. [27, p. 823] The equation for calculating the Bragg reflection wavelength λ_B is given by:

$$\lambda_B = \frac{n_{eff}\lambda_{uv}}{n_{uv}\sin(\theta/2)}, \quad (3.11)$$

where n_{eff} represents the effective mode index in the fiber, n_{uv} is the refractive index of silica in the UV, λ_{uv} stands for the wavelength of the inscription radiation, and θ denotes

the mutual angle of the UV beams. Since the mirrors are adjustable, the angle θ can range from 0° to 180° , allowing the Bragg wavelength to vary from the UV wavelength to theoretically infinity. [5, p. 54] However, a drawback of this approach is that it is slower compared to methods such as the phase mask inscription method.

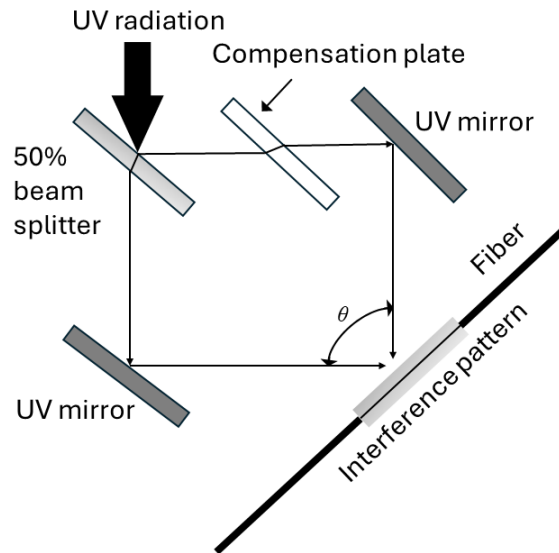


Figure 3.4. Schematics of UV interferometer. Adapted from [27, p. 823]

Another example of the interferometric technique is the phase mask interferometer where a similar approach to the phase mask is employed. The phase mask serves its primary function of diffracting light. However, to facilitate interference, rotatable and laterally translatable mirrors are built into the setup, which enables interference. This is illustrated in the Figure 3.5.

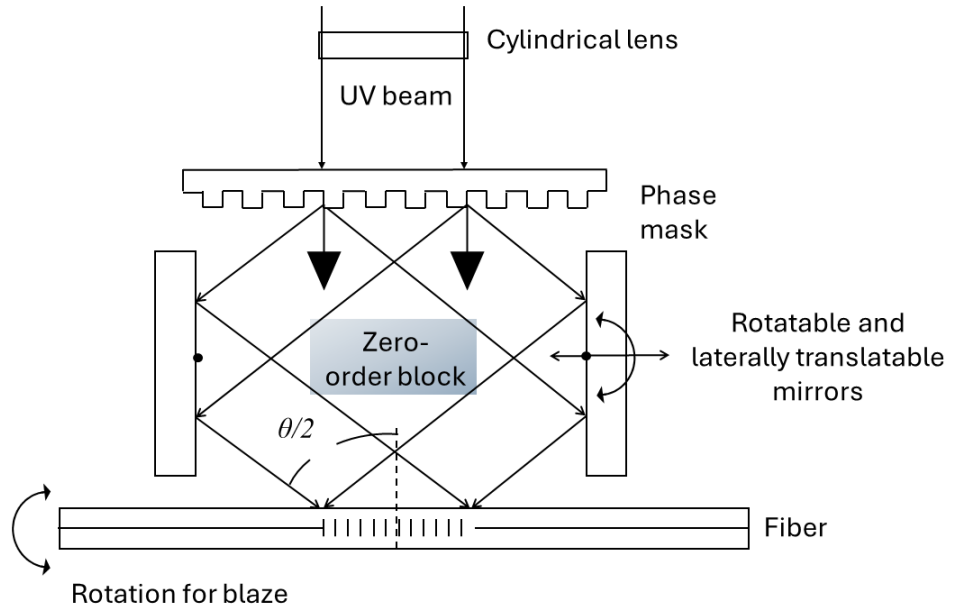


Figure 3.5. The schematics of the phase mask interferometer. Adapted from [5, p. 59]

The alteration of the Bragg wavelength is based on the change in the grating period by changing the mutual angle of the interfering beams. This is done by rotating the mirrors. The change in the Bragg wavelength can be derived by substituting equations 3.9 and 3.10 into 3.11

$$\frac{\Delta\lambda}{\lambda_B} = -\frac{\Delta\theta}{2} \cot(\theta/2). \quad [5, \text{p. } 60] \quad (3.12)$$

The phase mask interferometer can also be scanned to inscribe longer gratings, as noted in [5, p. 67]. This scanning capability, achieved by moving the UV beam, combined with the adjustability of the rotatable and laterally translatable mirrors enables the inscription of several different gratings. This makes the phase mask interferometer extremely versatile.

3.2.3 Point-by-point inscription method

The point-by-point inscription method is a non-interferometric technique involving the movement of a fiber along its axis relative to a laser beam. The period of the resulting grating depends on the speed at which the fiber moves and the repetition rate of a pulsed laser. Typically, an ultrashort-pulse (femtosecond) laser is used in the infrared or visible range. The principle behind this method is based on multiphoton absorption. However, maintaining consistent parameters and achieving reproducibility can be challenging due to the ultrahigh energy density of the pulses.

One advantage of the point-by-point method for writing is the ability to create Bragg structures with arbitrary periods without relying on phase masks or interferometers. Addition-

ally, complex Bragg structures such as chirped gratings and phased-shift gratings can also be inscribed using the point-by-point method.

4. DEVELOPMENT OF FBG FABRICATION PROCESS

Chapter 4 outlines the three key sub-processes essential for FBG fabrication: deuteration of the optical fiber, inscription of the FBG, and thermal annealing. This chapter focuses on how these processes were implemented in this work, along with a fourth critical sub-process, characterization, which serves as a quality control measure for the fabricated FBGs.

4.1 Deuteration of the optical fiber

This work employs a 100 ml deuterium chamber for the deuteration of the optical fiber using the cold, high-pressure deuteration method. Deuterium was chosen over hydrogen for reasons explained in Section 3.1.2. Before UV exposure, the fibers were placed in a chamber filled with deuterium gas and held under specific pressure and temperature conditions to saturate the fiber core with deuterium molecules. The pressure, temperature, and duration needed to achieve saturation were determined using the following equations.

Considering the known characteristics of deuterium, including its smaller diffusion coefficient [28, pp. 712-713] a comparison of between hydrogen and deuterium was conducted in cold loading process at 20°C and 125 bar. This can be computed by solving the diffusion equation in cylindrical coordinates, as expressed below:

$$C = C_{sat} \left(1 - 2 \sum_{n=1}^{\infty} \frac{1}{\beta_n J_1(\beta_n)} \exp \left(-D \left(\frac{\beta_n}{R} \right)^2 t \right) \right). \quad (4.1)$$

Here β_n is the n^{th} roots of the J_0 Bessel function, D denotes the diffusion coefficient 3.4, R stands for the optical fiber radius, and t is the duration of the hydrogenation/deuteration process. [5, p. 31], [18, p. 43]

The saturation concentration C_{sat} describes the maximum concentration that could be achieved during a hydrogenation/deuteration process. The saturation concentration for hydrogen/deuterium can be estimated by using the following Equation:

$$C_{sat} = 3.3481 P e^{(8670 J/mol/RT)}, \quad (4.2)$$

where P represents the pressure in atm, R is the gas constant, and denotes the temperature in Kelvin. It's important to note that 1 ppm is defined as 10^{-6} moles of H_2/D_2 per mole of SiO_2 [18, p. 43].

Figure 4.1 provides a visual illustration of the hydrogen/deuterium diffusion at 125 bar pressure, a typical pressure for the equipment utilized in this study, across varying temperatures.

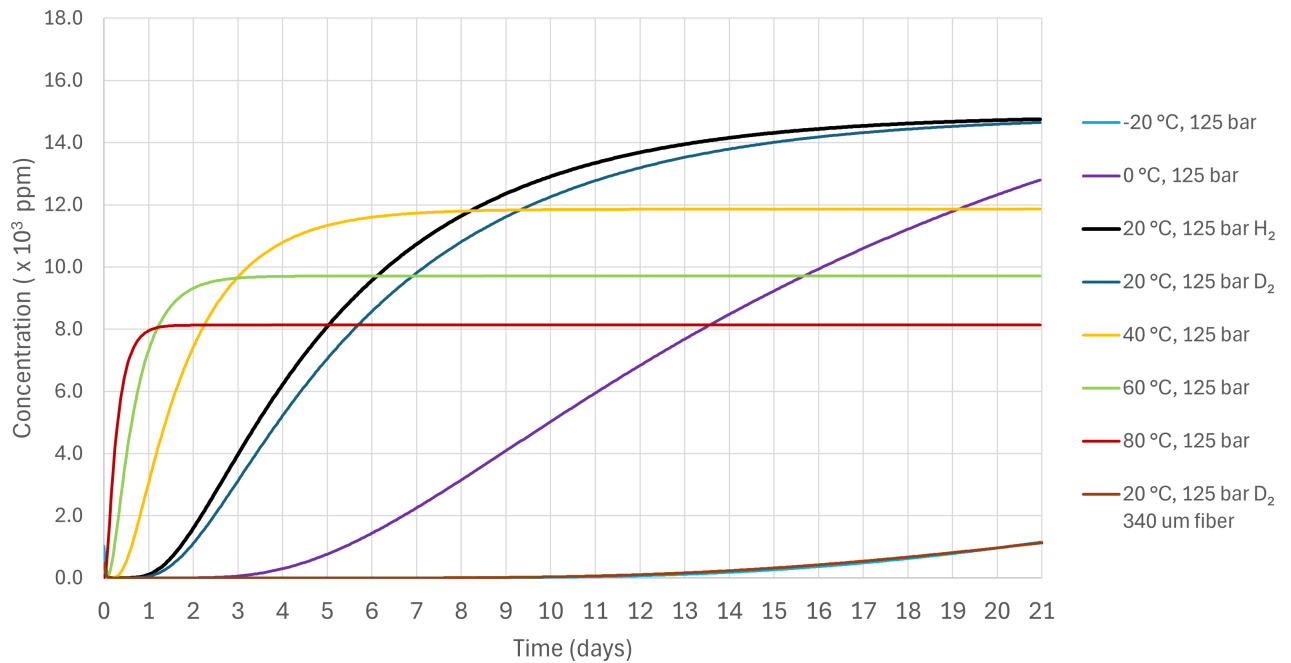


Figure 4.1. Illustration of the hydrogen and deuterium concentration development in various temperature and pressure conditions

As the temperature decreases, the saturation concentration increases, and at the same time, the time required to reach saturation also significantly increases. The graph suggests that the optimal conditions seem to be at 20 °C and 125 bar, with a deuteration period of 14 days, as mentioned in the concluding remarks of Section 3.1.2.

The graph suggests no significant change in the diffusion between hydrogen and deuterium in-diffusion. Storage at low temperatures is crucial to mitigate the potential out-diffusion of deuterium from the fiber, as detailed in Section 3.1.2.

4.2 FBG inscription

In this work, a scanning interferometric FBG inscription system was utilized for the fabrication of the FBGs 4.2. The system comprises the following essential equipment:

Inscription laser: A q-switched solid-state laser system with frequency conversion units, which convert the initial laser light at 1064 nm down to 213 nm serves as the primary laser source for FBG inscription. It is capable of inscribing FBGs in both deuterium-loaded fibers and non-deuterium-loaded Germanium-doped silica fibers, leveraging the absorption properties of $Ge(2)$ at that wavelength.

Optics: The FBG inscription setup includes various optics to direct the laser light into the interferometer which are illustrated in 4.2. There are two mirrors, labeled $M1$ and $M2$, which are used to raise the laser beam to a specific height to ensure horizontal alignment. Additionally, the setup has irises for alignment purposes. The first iris is positioned after mirror $M2$, followed by a shutter to control the laser light input into the inscription system. After that, the laser light passes through a second iris, labeled as $I2$, and is directed into the interferometer by a scanning mirror on top of a scanning motor.

Interferometer: The scanning interferometer is the main component used for inscribing Fiber Bragg Gratings (FBGs). It consists of a phase mask that generates a diffraction pattern. Two mirrors are then used to capture the first-order diffraction peaks and reflect them onto the fiber. These mirrors provide flexibility in movement and rotation, allowing precise control over beam positioning. The beams are focused onto the fiber, overlapping to enable FBG inscription. For a detailed understanding of the inscription process, please refer to Section 3.2.

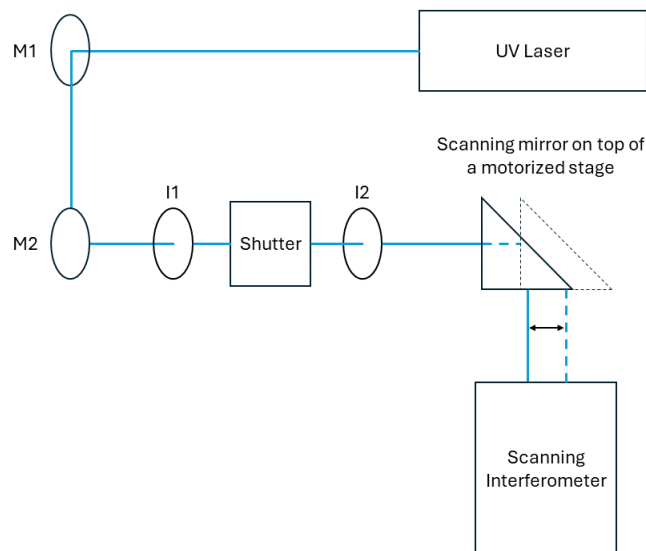


Figure 4.2. The illustration of FBG inscription setup.

The FBG inscription process involves several steps. Firstly, the photosensitized fibers are taken from the ultralow-temperature freezer. Then, a small portion of the polymer is peeled off using a scalpel, typically at least 20 mm, where the FBG is inscribed.

When creating a new fiber Bragg grating, it's important to understand the inscription parameters and how they affect the final results. Parameters such as laser power, FBG

length, scanning speed, apodization, and phase shift all impact the most, and therefore, they are under control and recorded for future reference for each fabricated FBG. The FBG spectrum during the inscription process is captured using an optical spectrum analyzer (OSA). To use the OSA, a characterization setup incorporating a wideband light source is required, which is detailed in subsection 4.4.1. Using the characterization setup requires preparing the fiber by removing the deuterium from the fiber ends. It is necessary because the electric arc during the splicing induces a small explosion inside the fiber ends, which ruins the splice. This process typically takes a couple of minutes on a hotplate in high temperatures for a standard single-mode fiber.

Once the fiber has been prepared and OSA is ready, the fiber can be fixed on the scanning interferometer for inscription. When determining the inscription parameters, it is also important to consider the Bragg wavelength shifts as deuterium out-diffuses from the optical fiber. This will be discussed in detail in Section 4.3.

To ensure a consistent inscription process, the growth of the grating must be recorded and analyzed to understand how specific parameters affect the final properties of the FBG. The growth is recorded with the characterization setup explained in Section 4.4.1. Consequently, when new types of gratings are developed, this knowledge helps to minimize the iteration cycle required for process refinement.

4.3 Thermal annealing of the FBG

Removing deuterium after inscribing it into the grating is commonly known as annealing. This procedure involves exposing the fiber Bragg grating to elevated temperatures under normal pressure conditions.

Annealing was conducted using a vacuum-drying oven. The fiber used was a standard single-mode fiber, with the wavelength inscribed at approximately 1550 nm. The data was collected with the equipment detailed in Section 4.4. Based on the estimation derived from Equation 3.7, the annealing test duration was determined to be 30 hours in a range of 50-100°C. A Python script was employed to record the trace of the OSA at 15-minute intervals. The shift of the FBG center wavelength during the annealing can be viewed from the following graph 4.3.

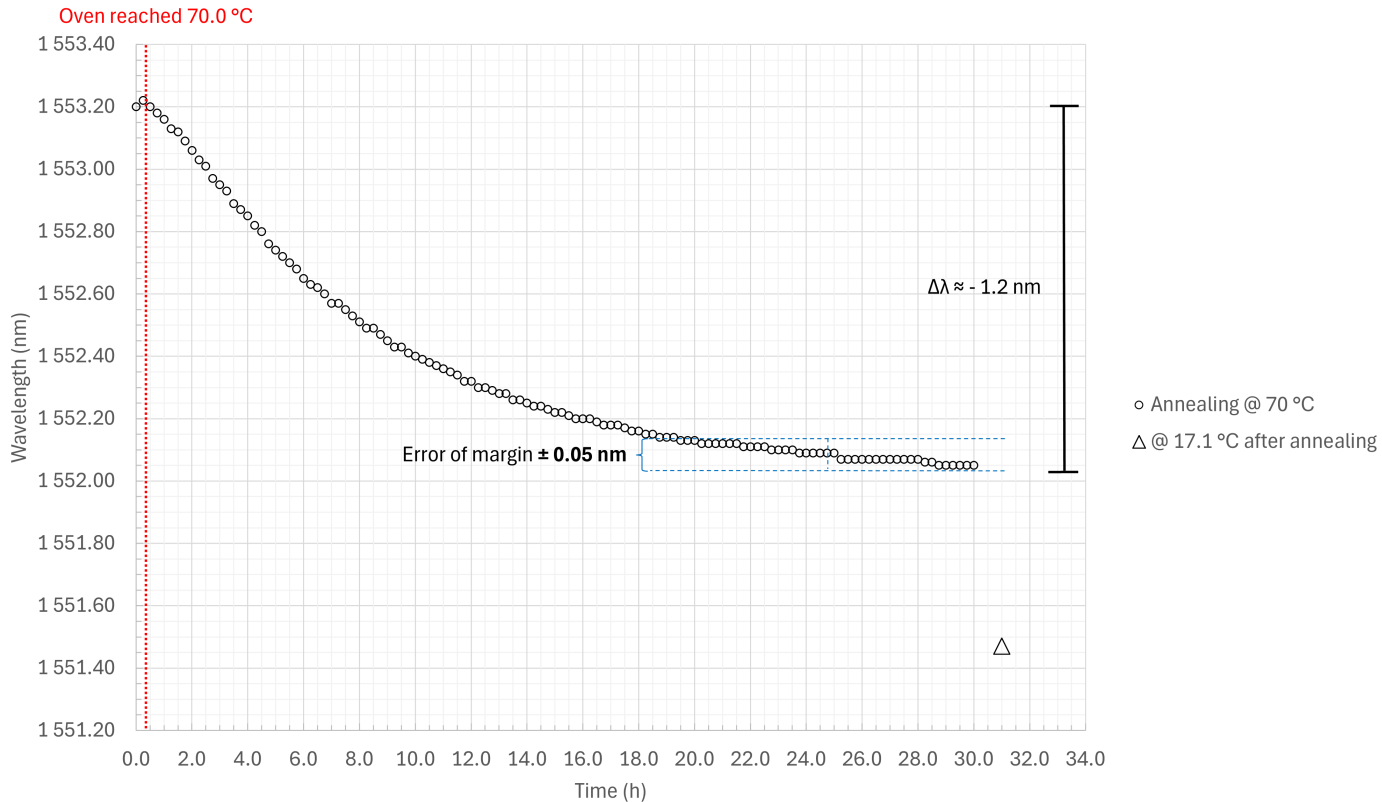


Figure 4.3. Annealing of the FBG in vacuum drying oven at 70 °C

The effects of annealing are observed in the shift of the Bragg wavelength in the reflectivity spectra of the FBG. The wavelength changes rapidly in the early hours of annealing, stabilizing around the 24-hour mark. Importantly, there is no temperature shift during the annealing process, so the temperature dependence of the FBG does not pose a problem to the results.

The observed wavelength shift during annealing is approximately -1.2 nm. It's important to note that the optical spectrum analyzer (OSA) used has a resolution of only 0.05 nm, which impacts the accuracy of measurements, particularly toward the end of the annealing process. At the 24-hour mark, it becomes apparent that within 12 hours, all measurements fall within the margin of error of the OSA. Consequently, towards the end of annealing, the observed change in wavelength diminishes to a mere 0.01 nm, making it insignificant.

Considering these limitations, it can be concluded that a minimum annealing time of 24 hours would be sufficient, resulting in a wavelength shift of approximately 1.2 nm towards shorter wavelengths. This observation aligns with the predictions derived from Equation 3.7. While specific shifts may vary depending on the fiber type used, any differences are expected to be minimal. Nonetheless, for applications requiring highly precise FBGs with narrow bandwidths at specific wavelengths, a similar procedure may need to be repeated to achieve desired outcomes.

It is noteworthy that the Bragg wavelength was measured after annealing, as indicated by the triangular marker in Figure 4.3. The temperature difference at the end of the annealing process and after it is $\Delta T = 51.9\text{ }^\circ\text{C}$, with a corresponding wavelength shift of $\Delta\lambda = 0.58\text{ nm}$. Using Equation 2.27, the sensitivity between these points can be approximately estimated as $K_{B,T} \approx 11\text{ pm}/^\circ\text{C}$. This value is reasonably close to the general calculated value presented in Section 2.3.1.

4.4 Characterization of the FBG

In the characterization of fiber Bragg gratings, three primary parameters describe their performance. Firstly, the center wavelength describes the specific wavelength at which the FBG reflects incident light most effectively, typically positioned at the midpoint of the spectrum. This parameter is a fundamental reference point for the FBG's spectral behavior. Secondly, the bandwidth characterizes the range of wavelengths over which significant reflection occurs, providing insights into the FBG's spectral selectivity. A narrower bandwidth implies a more precise response to incident light, while a broader bandwidth indicates a wider range of wavelengths for significant reflection. Lastly, the reflectivity quantifies the efficiency of light reflection from the FBG. Understanding and analyzing these key parameters are essential for optimizing the performance and deployment of FBGs in diverse optical and photonic systems.

4.4.1 Characterization setup

At the heart of the characterization process lies the Optical Spectrum Analyzer (OSA). A resolution of 0.05 nm across a wide spectral range plays a crucial role in the detailed analysis of Fiber Bragg Gratings (FBGs). Its high precision and wide applicability make it essential not only for characterizing FBGs but also for various analyses throughout different phases of the fabrication process.

A superluminescent diode (SLED) with a broad 150 nm bandwidth around 1550 nm is utilized to characterize FBGs in the 1550 nm region. It acts as a light source for OSA and enables their characterization.

To safeguard the equipment against back reflections from the Fiber Bragg Grating (FBG) and to facilitate the collection of reflectivity data, the introduction of a circulator into the system is necessary. Typically, optical circulators are constructed using a Faraday rotator sandwiched between two polarizers. Additionally, an optical circulator is utilized, capitalizing on the nonreciprocal polarization of an optical signal via the Faraday effect. These devices are three-terminal, with the input signal entering through terminal 1, the output exiting through terminal 2, and any reflected signal redirected to terminal 3 instead of returning to terminal 1. [29, pp. 353–356].

To complete the setup, the components are joined together directly using bare fiber or the fiber ends are connected to FC/APC (Ferrule Connector/Angled Physical Contact) connectors, which are then linked to other devices. You can see the entire setup illustrated in 4.4, where FBG is connected to terminal 2 of the circulator.

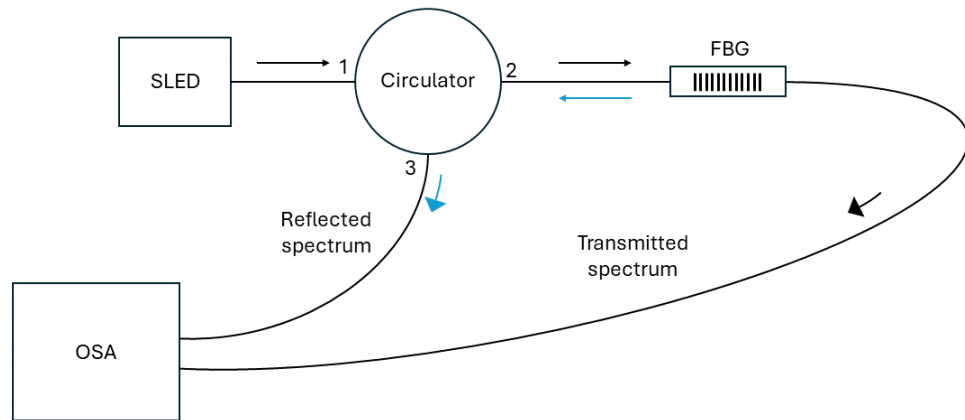


Figure 4.4. Illustration of the FBG characterization setup.

Depending on the spectrum to be measured, either the FBG is connected to the OSA or circulator's terminal 3 is connected to the OSA. If the FBG is connected, then the transmission spectrum is being measured and if the circulator's terminal 3 is connected, then the reflected spectrum is being measured.

4.4.2 Analysis of the characterization data

The center wavelength is found by analyzing the reflectivity spectrum of the FBG. Since the spectrum may not always be symmetrical, the center wavelength is identified as the midpoint position where the reflectivity decreases to 3 dB (50%) below its maximum value. This approach helps to accurately capture the spectral position where reflection is at its peak.

The bandwidth of a fiber Bragg grating is determined from the reflectivity spectrum and refers to the range of wavelengths over which significant reflection occurs. In the reflectivity spectrum, the bandwidth corresponds to the spectral width of the peak. To quantify this, we typically measure the linewidth at the 3 dB point from the maximum reflectivity, which means we determine the width of the spectrum where the reflectivity drops to half of its maximum value. This approach provides a standardized method for characterizing the spectral selectivity of the FBG.

The reflectivity of the FBG is determined by its transmission spectrum. However, to accurately measure the reflectivity, the baseline of the superluminescent diode needs to be subtracted from the transmission spectrum. This baseline represents the inherent noise

or background signal of the system, ensuring that only the signal from the FBG itself is considered. After subtracting the baseline, we calculate the transmission depth (T) in dB, which represents the fraction of incident light that is transmitted through the FBG. Then, we can calculate the reflectivity (R) as a percentage using the following equation

$$R = 1 - 10^{-T/10}, \quad (4.3)$$

where (T) is always considered as a positive number [30, p. 26474].

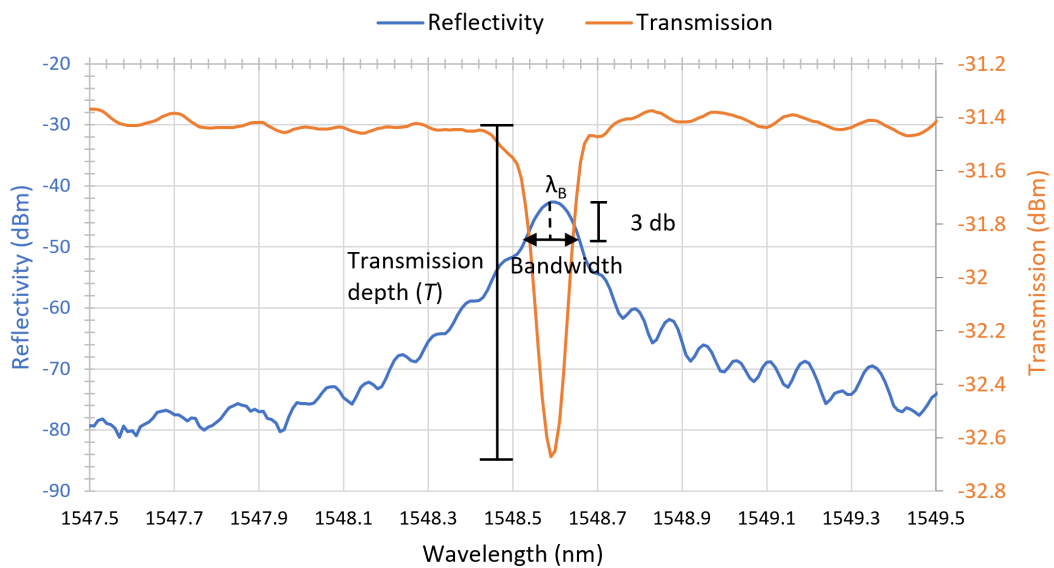


Figure 4.5. Transmission and reflectivity spectrum of an example FBG with illustrative definitions for transmission depth, bandwidth, and Bragg wavelength λ_B

Transmission and reflectivity spectra are plotted in Figure 4.5. Following the spectral data collection, a Python script calculates all the parameters described earlier. Analysis results in the center wavelength being 1548.58 nm, bandwidth being 0.1 nm, and the reflectivity being 26.1%.

5. IMPLEMENTATION OF FBG INSCRIBED IN A LARGE DIAMETER OPTICAL FIBER AS A TEMPERATURE SENSOR

As discussed in Section 2.3, fiber Bragg gratings find applications in various sensing contexts, with temperature sensing being the focus of this work. This chapter concentrates on fabricating FBG in a thick optical fiber with a diameter of 400 μm . Furthermore, the fabricated FBG is analyzed to evaluate its performance as a temperature sensor, using a commercial temperature sensor as a reference.

5.1 Methodology for FBG characterization

The measurement setup used for analyzing the temperature sensor differs slightly from the setup described in sub-section 4.4.1. The main difference is that the interrogator is used instead of OSA because the resolution of the interrogator is better for precise wavelength monitoring.

The interrogator is the core component of the FBG sensing system, facilitating real-time spectrum monitoring of FBG sensors. This study utilizes a high-resolution interrogator platform that functions by comparing the light detected by its photodetectors with reference artifacts [31]. The interrogator features multiple transmission gratings housed in a compact unit, allowing for the spatial separation of the wavelength spectrum. This separation enables accurate determination of the reflected FBG wavelengths by using peak fitting algorithms, which enhances the reliability of temperature measurements.

5.2 Analysis of commercial temperature sensor

Analyzing the temperature response of the inscribed FBG is essential for assessing its performance. This analysis involved using a commercial fiber Bragg grating temperature sensor as a reference point. The measurements to define reference was done as follows: measurements were recorded simultaneously over time, complete with timestamps. The temperature data for the FBG was obtained using a digital thermometer placed beneath the FBG in an open container filled with water, while the Bragg wavelength was monitored

using the interrogator. The measurement setup is illustrated in Figure 5.6.



Figure 5.1. Temperature measurement setup for commercial sensor

The FBG was placed in heated water, causing a rapid increase in temperature. However, due to the slow response time of the Digital Thermometer Prima Long Amarell (8 seconds) and the separate data collection for temperature and wavelength, the heating phase couldn't be measured reliably. Therefore, the cooling phase of the water was used to determine the sensitivity of the commercial FBG. After 60 seconds of heating, the temperature began to stabilize. From that point onward, the water cooled down through convection. The temperature measured with a digital thermometer and wavelength measured with an interrogator can be seen in Figure 5.2.

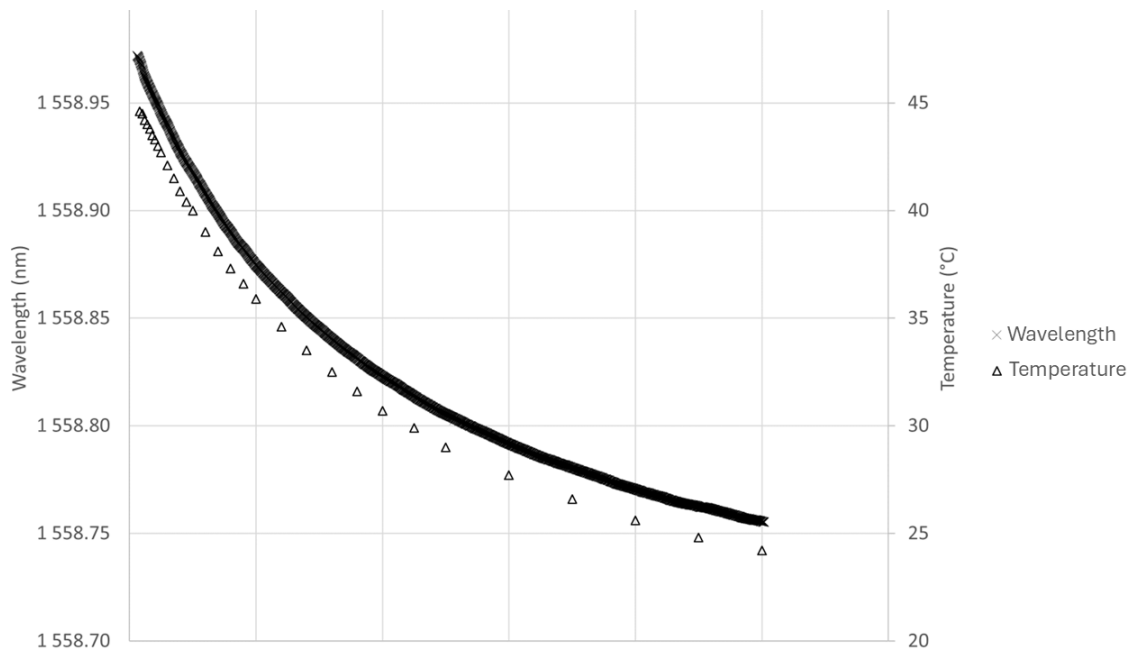


Figure 5.2. Measured temperature and wavelength response of the commercial temperature sensor

The cooling phase unfolds gradually, spanning approximately 5000 seconds to return to

its initial temperature. Remarkably, during the cooling process, the temperature changes occur at such minute time scales that the slow response time of the thermometer becomes irrelevant. This mitigates the challenge posed by the slow response time of the thermometer.

5.2.1 Temperature sensitivity analysis

Using the data from figure 5.2, it is possible to construct a wavelength-temperature dependent graph 5.3. The graph shows a clear linear relationship between wavelength and temperature, as described by equation 2.28. This enables us to derive a sensitivity of $10.3 \text{ pm}/^\circ\text{C}$ directly from the slope. However, to ensure precise sensitivity determination and reliable results, conducting an error analysis of the collected data is essential. This analysis will help identify and quantify any potential sources of error, ensuring the accuracy and validity of the findings.

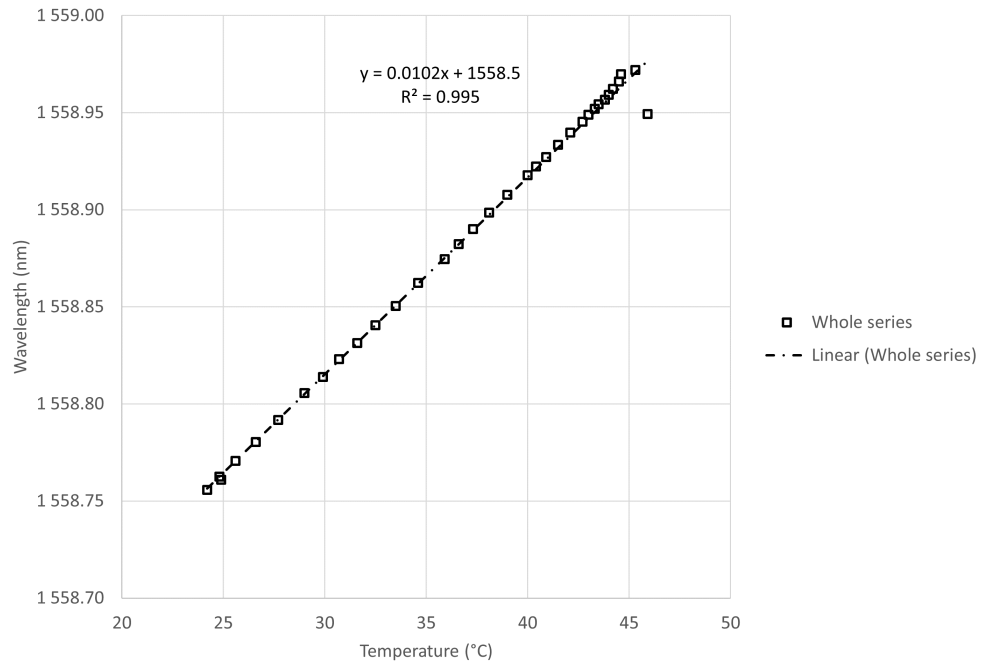


Figure 5.3. Temperature-wavelength graph shows linear dependent for the commercial temperature sensor

To estimate the maximum potential error in sensitivity, we employ the general formula for error propagation [32, p. 75], represented by equation 5.1

$$\begin{aligned}
|\Delta K_{B,T}| &\leq \left| \frac{\partial K_{B,T}}{\partial T} \right| \sigma_T + \left| \frac{\partial K_{B,T}}{\partial \lambda} \right| \sigma_\lambda \\
&= \left| \frac{-\Delta \lambda_B}{(\Delta T)^2} \right| \sigma_T + \left| \frac{1}{\Delta T} \right| \sigma_\lambda \\
&= \left| \frac{1}{\Delta T} \right| (K_{B,T} \sigma_T + \sigma_\lambda),
\end{aligned} \tag{5.1}$$

where $\Delta K_{B,T}$ signifies the error in sensitivity, while $K_{B,T}$ denotes the sensitivity itself. Furthermore, σ_T represents the measurement error in temperature, and σ_λ refers to the measurement error in wavelength. Notably, ΔT signifies the temperature range over which the sensitivity $K_{B,T}$ is determined.

The known measurement errors for the interrogator and thermometer are $\sigma_\lambda = 5$ pm and $\sigma_T = 1$ °C, respectively. Utilizing the slope of the graph in Figure 5.3 and the temperature range $\Delta T = 21.7$ °C, we determine the sensitivity of the FBG, $K_{B,T} = 10.3$ pm/°C. Substituting these values into Equation 5.1, we calculate the error in sensitivity to be $\Delta K_{B,T} = 0.705$ pm/°C.

Now that the error in defining the sensitivity is known, we can determine the measurement error $\sigma_{T'}$ in temperature for the commercial FBG using Equation 5.2.

$$\sigma_{T'} = \frac{\sigma_\lambda}{K_{B,T}}. \tag{5.2}$$

With a sensitivity of $K_{B,T} = 10.3 \pm 0.705$ pm/°C, the resulting temperature accuracy is calculated as $\sigma_{T'} = 0.488 \pm 0.033$ °C, yielding an overall value of 0.521 °C. This result is considered suitable for most applications. However, for scenarios requiring higher measurement accuracy, enhancements to either the sensitivity of the FBG or the resolution of the interrogator would be necessary.

It is important to note that while changes in temperature accuracy σ_T may influence the sensitivity value, their impact on overall measurement accuracy $\sigma_{T'}$ is minimal. For instance, with a temperature measurement accuracy of $\sigma_T = 0.1$ °C, the resulting FBG measurement accuracy would be $\sigma_{T'} = 0.486 (\pm) 0.013$ °C, amounting to 0.499 °C. This adjustment would lead to an approximate 4% increase in temperature accuracy, highlighting the significance of precision enhancements in temperature measurement systems.

5.3 FBG-based temperature sensor in a large diameter optical fiber

As discussed in Section 2.3, fiber Bragg gratings are used in various sensing applications, with a focus on temperature sensing in this study. The performance of a commercial temperature sensor is compared to that of a fabricated FBG. This chapter also includes an

analysis of typical factors affecting the measurement accuracy of FBG-based temperature sensors. The FBG is inscribed into a 400 μm diameter optical fiber.

In addition to the temperature sensitivity measurements, the different factors that introduce measurement accuracy errors are also analyzed. The most important factors are stress, bending, and distance from the measurement point.

5.3.1 Fabrication and characterization of FBG

The deuterium-loading of 400 μm optical fiber follows the same protocol outlined in Section 4.1. According to Equation 4.1, an increase in fiber diameter results in a decrease in deuterium concentration. This is visually represented in Figure 5.4 where it is evident that the loading time experiences a significant increase to reach the saturation point as the fiber diameter increases from 125 μm into 400 μm .

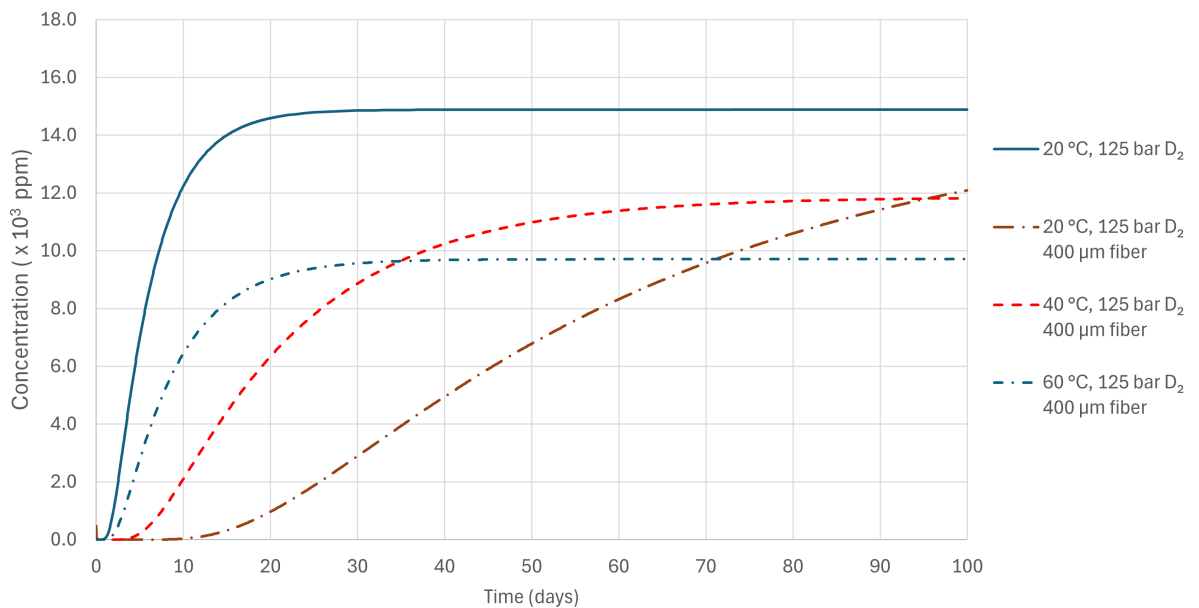


Figure 5.4. Calculated deuterium concentration for 400 μm diameter optical fiber based on the diffusion model 4.1

The inscription of the fiber followed the same principles as mentioned in Section 4.2. Against expectations, it was noticeable that the FBG grows even with lower inscription power levels, which means that adjusting the inscription power level and duration mainly affects the reflectivity of the grating. After the inscription, the optical fiber underwent the annealing process identical as in Section 4.3, which was 30 hours at 70 °C. It was not enough, because if the deuterium-loading (in-diffusion) takes longer with a larger diameter, so does the out-diffusion. Figure 5.5 illustrates the effect of fiber diameter and

temperature to the out-diffusion of deuterium based on Equation 3.6.

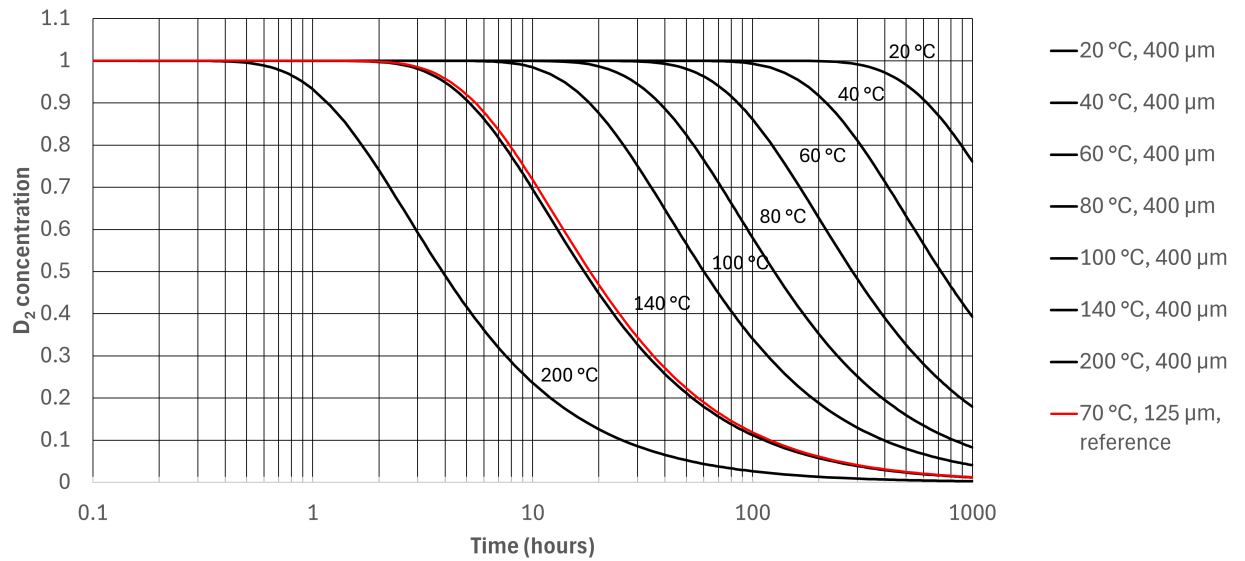


Figure 5.5. Illustration of out-diffusion based on theoretical model

A noteworthy mention is that the total combination of deuterium loading process parameters and annealing affects the total deuterium level in the optical fiber after processing. When comparing the theoretical model to the results in Section 4.3 for standard fiber, it can be concluded that subjecting a 400 μm optical fiber to annealing at 30 hours at 140 $^{\circ}\text{C}$ should produce the same results as standard optical fiber processed for the same duration at 70 $^{\circ}\text{C}$.

5.3.2 FBG temperature sensitivity

The primary focus of this subsection is to analyze the temperature sensitivity of the FBG inscribed in the 400 μm diameter optical fiber. The FBG is sensitive to various factors, as explained in Section 2.3, all of which need to be considered. The most significant factors to consider are temperature, bending, and stress. The detailed analysis of stress and bending factors is confidential and not included in the thesis.

Figure 5.6 provides an overview of the measurement setup used to measure the temperature of the FBG.

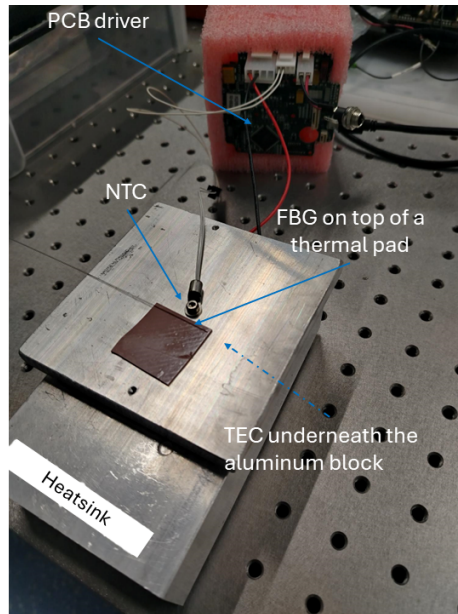


Figure 5.6. Temperature measurement setup for sensitivity

A thermoelectric cooler (TEC) controls the temperature in the measurement setup. It lays on a heatsink for dissipation of heat which enables accurate control of the temperature during measurements. Atop TEC lies an aluminum block with a negative temperature coefficient (NTC) thermistor attached to it to measure the temperature. A printed circuit board (PCB) driver records the temperature data with timestamps. At the same time, an interrogator was used to capture the reflected wavelength from the FBG.

For accurate temperature measurement, it is crucial to minimize bending and stress. This can be achieved by placing the fiber Bragg grating straight on top of a thermal pad and next to the NTC thermistor. This arrangement enhances heat transfer to the FBG, reducing the time for heat to transfer into the core of the glass fiber. Therefore direct contact with the heat source generally reduces the FBG sensor's reaction time. As a result, both components can reach and maintain the same temperature with minimal differences.

The measurement was collected using the interrogator to log on the FBG wavelength data and the PCB driver was used to log the temperature data of the NTC. The following Figure 5.7 shows the wavelength and temperature development during the measurement.

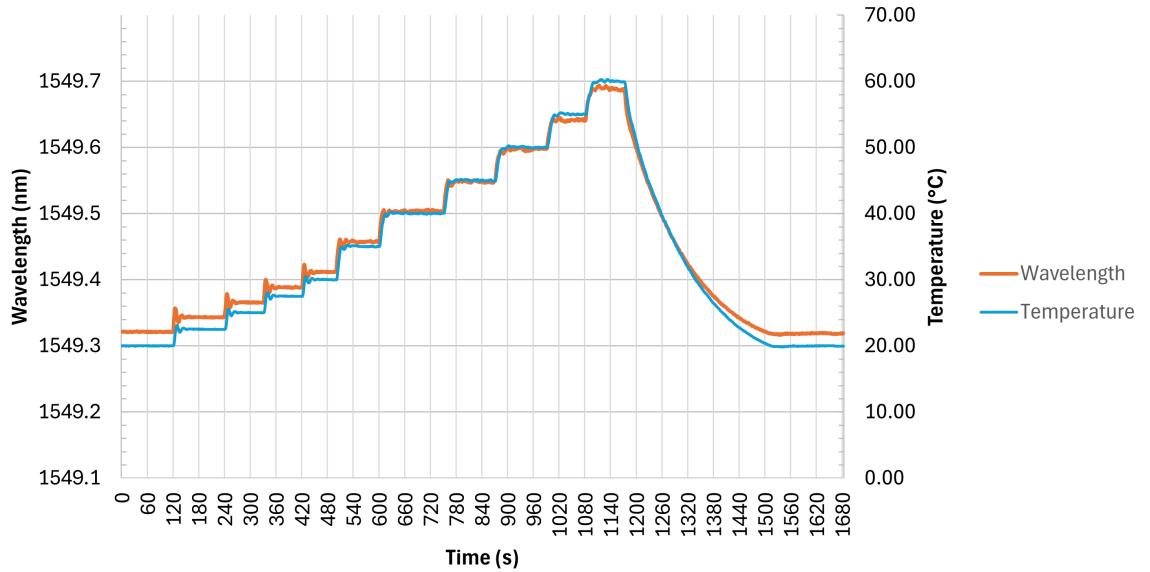


Figure 5.7. Temperature and Bragg wavelength measurement against time

The data logging had a 2-second delay between measurements, which was accounted for during the analysis. The measurement included a heating phase and a cooling phase. During the heating phase, the temperature was raised incrementally by 2.5 °C between 20-30 °C and then by 5.0 °C increments for the rest of the phase. After each increment, the temperature was allowed to stabilize. It is evident that during the heating period, the temperature and wavelength oscillated, which could be used to determine the sensor's response time in this environment.

Subsequently, at the end of the measurement, the temperature was set to decrease from 60 °C to 20 °C. This cooling phase occurs much more steadily. These phenomena become apparent when examining the wavelength data plotted against temperature, as illustrated in Figure 5.8.

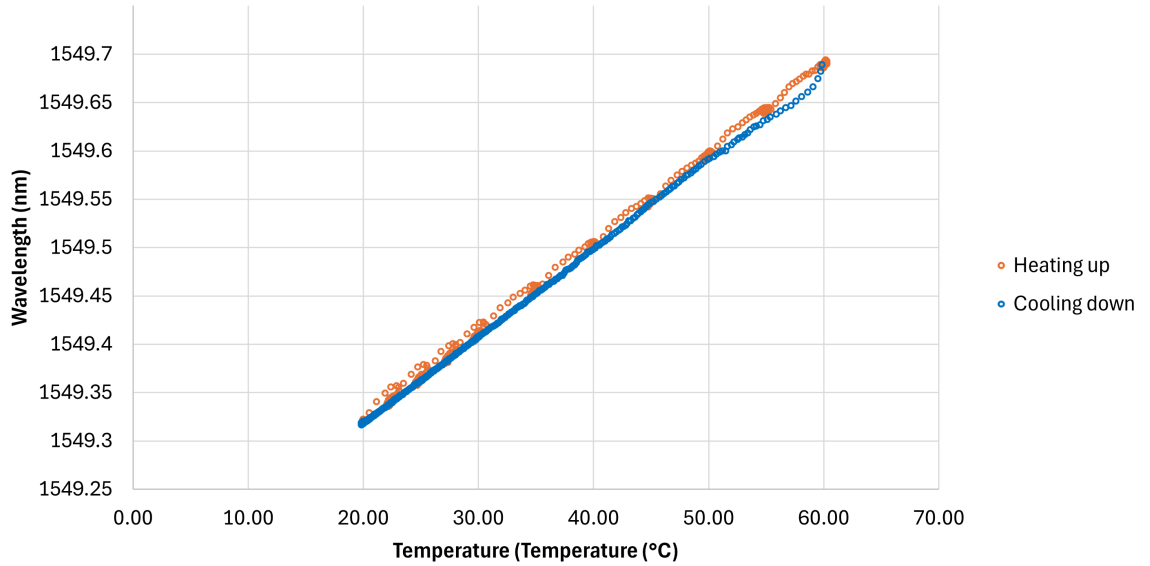


Figure 5.8. Temperature sensor wavelength as a function of temperature

In the heating phase, the data shows oscillations around specific points that display a linear alignment. It becomes evident later that the curls are unstable measurement points due to the delay in the response from FBG. During the cooling phase, the behavior becomes linear indicating a more stable change in temperature. Sensitivity is defined by focusing on stabilized values. Removing the unstable values from the graph 5.8 results in the following graph 5.9.

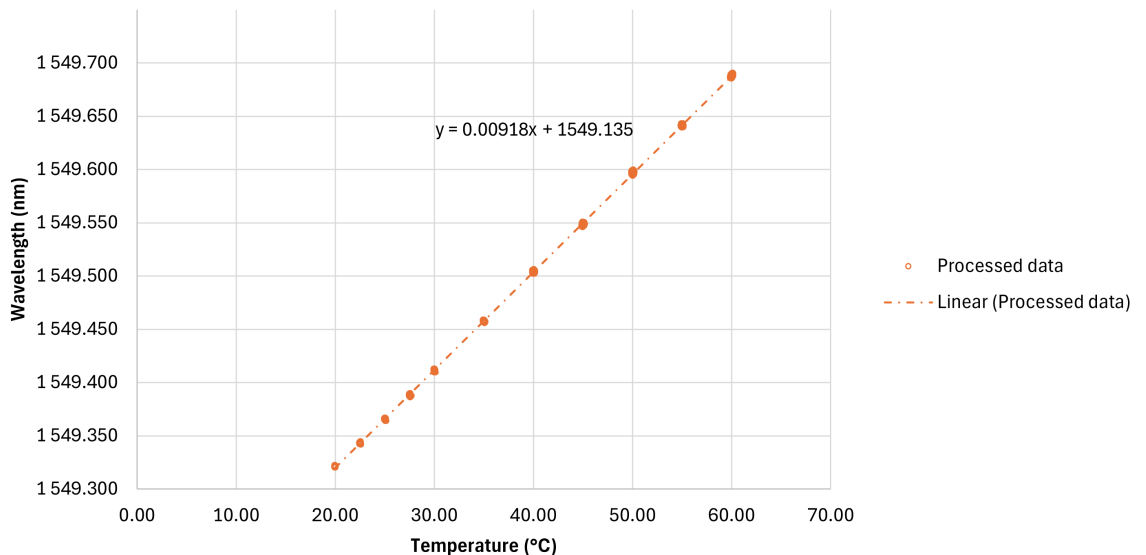


Figure 5.9. Processed data from graph 5.8 with only stabilized values

It is evident that with the stabilized values, the temperature and wavelength dependency exhibit a linear relationship. By following the procedures outlined in Section 5.2.1, the following results can be concluded: The measurement errors for interrogator and NTC

are $\sigma_\lambda = 5 \text{ pm}$ and $\sigma_T = 0.5 \text{ }^\circ\text{C}$, the measured temperature range is $\Delta T = 40.43 \text{ }^\circ\text{C}$. These values will result in sensitivity of $K_{B,T} = 9.18 \text{ pm}/^\circ\text{C}$ with an error of $\Delta K_{B,T} = 0.237 \text{ pm}/^\circ\text{C}$. With a sensitivity of $K_{B,T} = 9.18 \pm 0.237 \text{ pm}/^\circ\text{C}$, the resulting temperature accuracy is calculated to be $\sigma_{T'} = 0.545 (\pm) 0.014 \text{ }^\circ\text{C}$, yielding an overall accuracy of $0.55 \text{ }^\circ\text{C}$.

From the graph 5.9, it is possible to acquire the following relation for converging the wavelength into temperature

$$T = 108.932(\lambda_B - 1549.137) \quad (5.3)$$

where T is the converged temperature in $^\circ\text{C}$ and λ_B is the measured Bragg wavelength. This allows the DCOF to act as a temperature sensor by converting the analyzed wavelength to temperature.

With this conversion, it's possible to determine the response time in ideal conditions without outer factors such as bending or stress. When the first increment in the data in 5.7 is analyzed, and the actual temperature is compared to the converted temperature, the following graph 5.10 can be made.

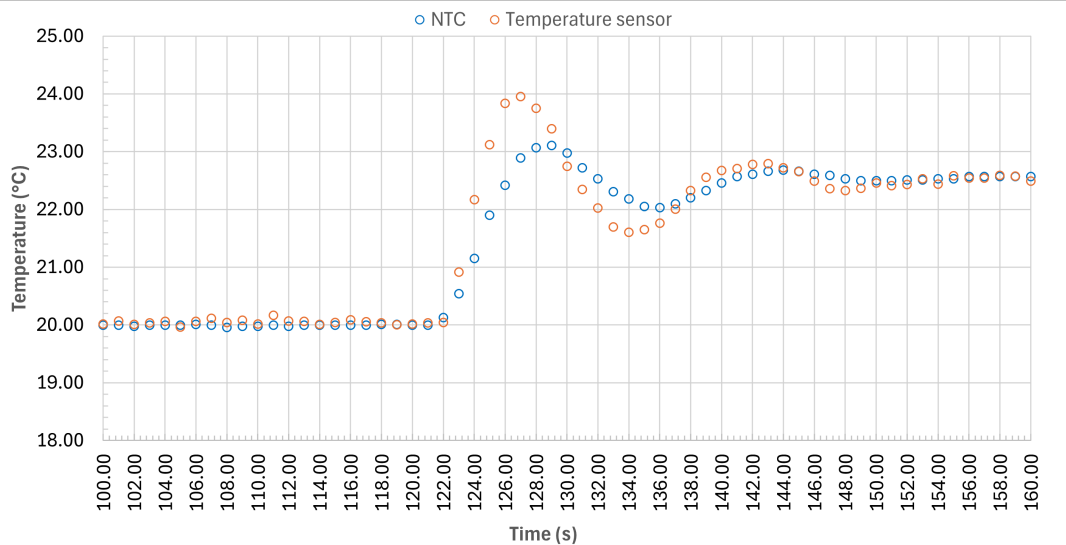


Figure 5.10. Response time in $2.5 \text{ }^\circ\text{C}$ temperature increment

It can be seen from the data that within the two first oscillations the response time is around two seconds while the oscillation keeps dampening. The temperature difference during this oscillation reaches up to $1.5 \text{ }^\circ\text{C}$ difference in the temperature. This delay will cause the temperature sensor to give quite a large error signal during the measurements, which can be seen when the deviation from the actual temperature is plotted in Figure 5.11.

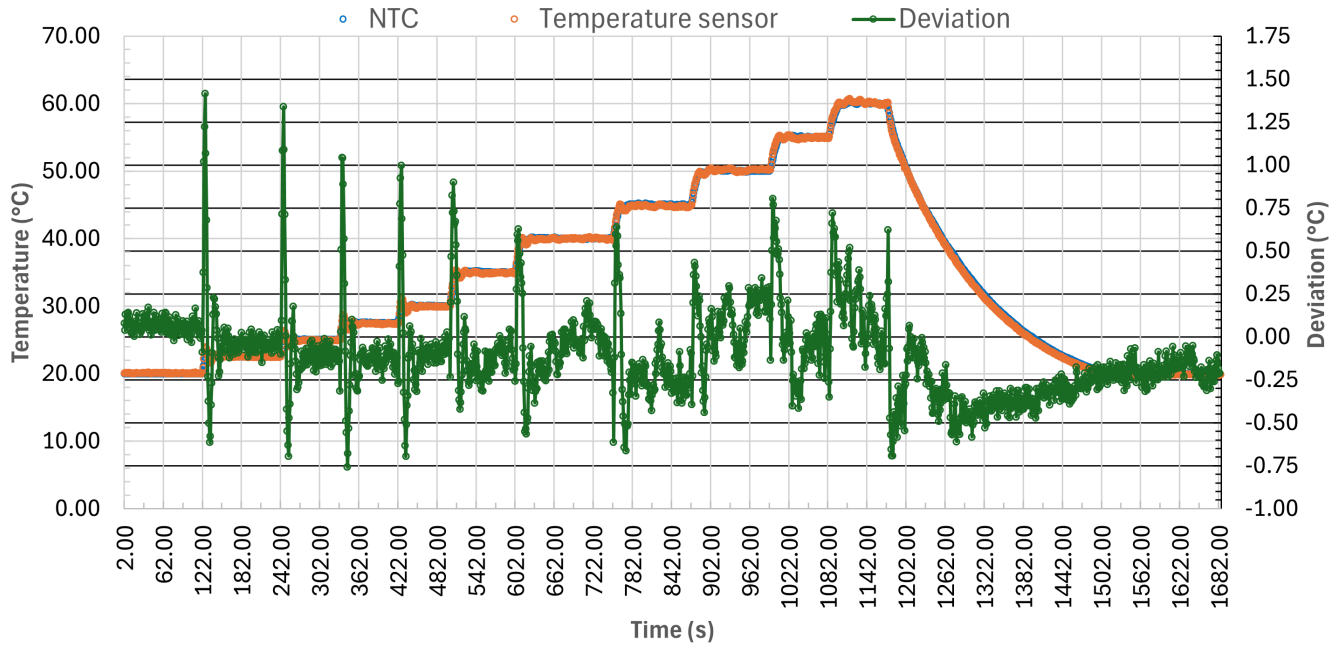


Figure 5.11. Temperature measurement response time and deviation

The FBG takes some time to stabilize during the increments, resulting in temperature values deviating from each other. It can be seen that in the range of 20–40°C, the temperature mostly stays within $\pm 0.25^\circ\text{C}$. In the higher temperatures of 40–60°C, it mostly stays within the range of $\pm 0.5^\circ\text{C}$. A detailed analysis of the first increment reveals that it takes 14 seconds for the temperature to reach the $\pm 0.25^\circ\text{C}$ range. In conclusion, the temperature sensor provides temperature measurements within the 20–60°C range with a precision of $\pm 0.50^\circ\text{C}$, while exhibiting a 14-second response time to incremental temperature changes. This assumes that the NTC provides absolute value readings.

It is important to note that during the initial stages of the measurement, there is a higher degree of deviation, while during the later stages, the deviation decreases. At approximately 25°C, the readings closely align with those of the NTC. This can be attributed to the method by which the NTC assesses temperature, employing a linear approximation around 25°C. Consequently, this approach results in inaccurate temperature measurements when the temperature exceeds or falls below 25°C, impacting the overall temperature measurement accuracy. To achieve more precise results, the implementation of the Steinhart–Hart equation is recommended, although this exceeds the scope of the present study (see [33, p. 2260]).

In summary, the sensor's sensitivity is sufficiently good, and Equation 5.3 can be used to determine the temperature. The response time of the FBG will always be influenced by the heat conductivity of the glass and the surrounding medium. This response time is greatly influenced by the measurement setup, so conducting a test measurement that replicates the application environment is crucial.

5.3.3 FBG temperature sensitivity depending on the distance from the measurement point

The FBG responds only to the temperature changes in the optical fiber. Therefore the distance between the measurement point and the FBG affects to temperature response of fiber Bragg grating. Depending on the application, the FBG might be placed directly against the measurement point/surface or there might be some gaps between the points.

This subchapter studies the effect of the distance between the measurement point and the FBG on the temperature response. Because the air has poor heat conductivity, there will be a critical distance, denoted as d_c , at which the temperature results will deviate significantly from the actual temperature values. This critical value can be determined by measuring the wavelength difference from the Fiber Bragg Grating (FBG) when the distance from a stable heat source is introduced. The measurement setup is illustrated in Figure 5.12.

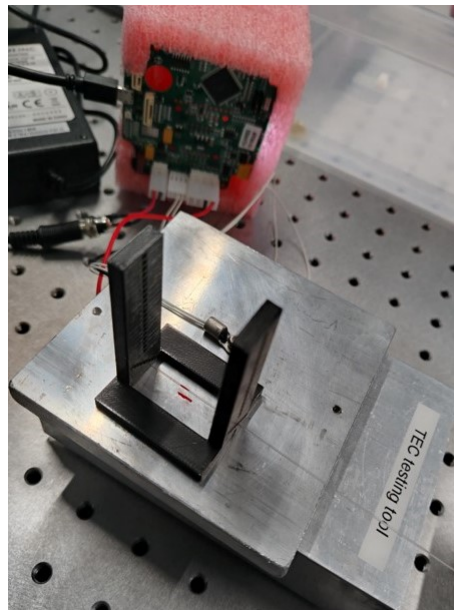


Figure 5.12. Measurement setup for determining the wavelength shift due to the distance

The experiment involved maintaining the aluminum block at a consistent temperature of 30 °C. Data was gathered using a 3D-printed holder with apertures at various heights to hold the fiber in place. The fiber was consistently placed at the same position for each measurement, and the wavelength was allowed to stabilize at each distance. Due to the limitations of 3D printing in achieving high accuracy, the heights of the apertures were measured using a thrust gauge. The wavelength data, along with the corresponding stabilization times, were recorded. Figure 5.13 illustrates the collected wavelength data.

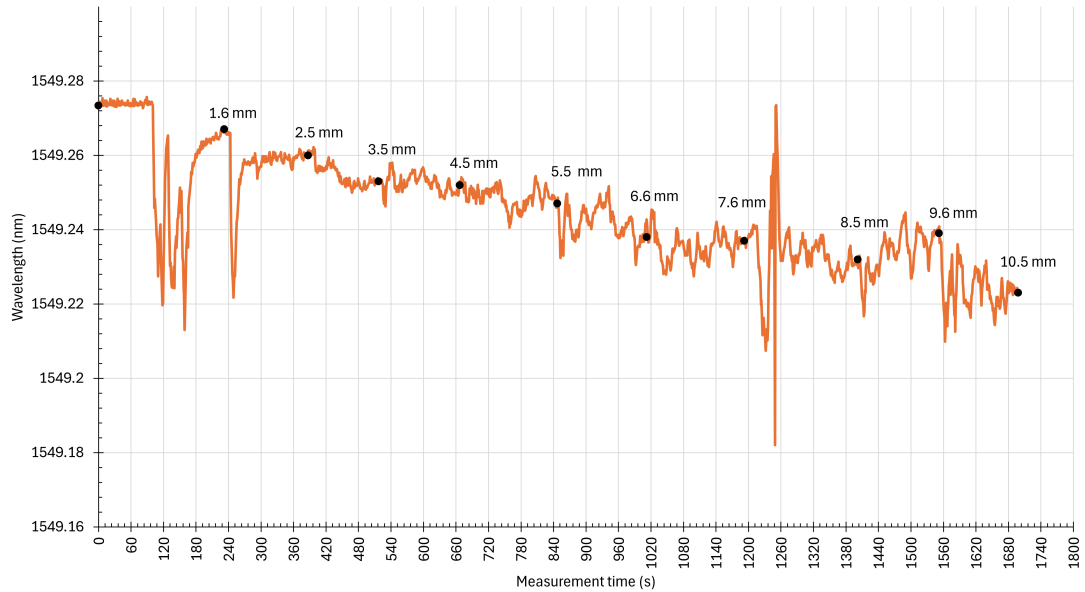


Figure 5.13. Wavelength response in time to the varied distance from measurement point

In the graph, the distances from the heat source were plotted as data points. The data illustrates that as the distance from the heat source increases, the wavelength decreases. Additionally, it is evident that as the distance increases, the wavelength measurements become less stable. This instability can be attributed to the experimental setup not being enclosed, leading to airflow-induced interference. Furthermore, the handling of the fiber optic cable contributed to significant spikes in the results, possibly due to instances where the fiber got stuck while being pushed or pulled, causing stress and bending. The dependency of wavelength on distance is depicted in the graph 5.14.

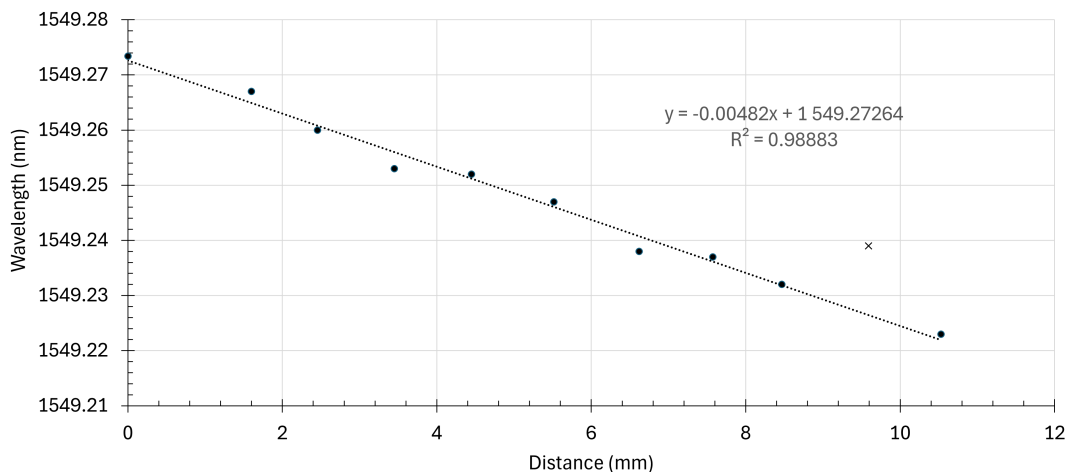


Figure 5.14. Bragg wavelength shift dependency on the distance from measurement point

The measured values show a linear dependency in this temperature range, except for one measurement error (marked as x in the graph). The rest of the data demonstrate high linearity, especially under these measurement conditions and distances. From the graph,

we can conclude that the error in the wavelength is approximately -4.82 pm/mm . This means that when the fiber is not attached to the sample, we will obtain lower temperature values than the actual temperature. This error is relatively high compared to the sensitivity of the fiber itself, which is 9.18 pm/C . It implies that a 2 mm distance corresponds to a 1 °C error in the measurement accuracy, making this the critical distance, $d_c = 2 \text{ mm}$.

Depending on the temperature difference in the heated aluminum block and the ambient temperature, the behavior might be different. These measurements should be done by imitating the most probable temperature value to see the proper behavior.

6. CONCLUSIONS

This work's goals were to develop and optimize the fabrication process for fiber Bragg gratings using interferometric methods to ensure reliable and predictable FBG fabrication. A secondary objective was to fabricate and evaluate the sensing capabilities of large-diameter FBGs.

The optimization of the FBG fabrication process proved successful, and the behavior of the FBGs growing process is now well understood, ensuring repeatability in production. The deuterium loading process performed as expected under the modeled parameters: fibers were placed in a deuterium loading chamber for two weeks at ambient temperature and pressure of 125 bars. Moreover, the same parameters applied during the FBG inscription process showed consistent repeatability, and the growth behaviors of the gratings were systematically recorded. Thermal annealing of the FBGs was also monitored, and the wavelength shifts observed during annealing were consistent and predictable.

To enhance process repeatability, several factors must be addressed. Currently, the deuteration level is managed solely through adjustments to deuterium loading time and pressure, as it is not directly measured. Variations in deuteration levels can influence the Bragg wavelength shift during annealing, which presents challenges for applications requiring precise control over bandwidth and Bragg wavelength. Developing a method to measure or monitor the deuterium concentration would significantly improve the repeatability of the process. One potential strategy is to deuterate multiple fibers simultaneously, fabricating one as a baseline to use as a reference. Furthermore, the fabrication process is sensitive to fiber parameters, indicating that each fiber type requires an individualized approach to processing.

The secondary goal of this thesis was to fabricate and evaluate the sensing capabilities of large-diameter FBGs. These FBGs were fabricated using a process similar to that for standard 125 μm optical fibers but with modified parameters. The fabricated FBGs showed promising performance, achieving a temperature measurement accuracy of $\sigma_{T'} = 0.55^\circ\text{C}$ when it was compared to a commercial FBG with measurement accuracy of $\sigma_{T'} = 0.50^\circ\text{C}$. While the measurement accuracy of the large-diameter FBGs was slightly worse, the thicker fibers offer advantages for robust sensing applications. Moreover, the stress response of the large-diameter FBGs was found to be highly sensitive,

particularly to bending, requiring careful strain control.

The demonstration and results gathered during this work suggest that this sensor could be used in various sensor applications. Depending on the application, some implementations need to be taken into account. For temperature sensing applications, a rigid body around the FBG would be essential to mitigate the strain and bending effects. For stress sensor applications, an additional FBG would suffice for measurements. Since the first FBG is strain compensated, the wavelength difference between these FBGs would give the actual strain. It is important to note that this kind of sensor does not have the best response time, as usually the sensor and measurement point have air between them, and air is a poor heat conductor. Due to the large diameter of the fiber, it is much sturdier than standard fiber. Therefore, it could be used in different applications that would benefit from this, such as uncontrolled stress and bend measurements. This is possible since the temperature response to stress and bending is known, and it just results in measurement accuracy errors.

Overall, this work has demonstrated the successful optimization of a systematic and reliable process for FBG fabrication and highlighted the potential of large-diameter FBGs for robust and precise sensing applications.

REFERENCES

- [1] STL. *Types Of Optical Fiber*. [Accessed: 13-Nov-2023]. URL: <https://stl.tech/blog/types-of-optical-fiber/>.
- [2] FOSCO. *GEOMETRICAL-OPTICS DESCRIPTION OF STEP-INDEX AND GRADED-INDEX OPTICAL FIBERS*. [Accessed: 13-Nov-2023]. URL: <https://www.fiberoptics4sale.com/blogs/wave-optics/step-index-optical-fibers>.
- [3] FS Community. *Step-Index Multimode Fiber vs Graded-Index Multimode Fiber*. [Accessed: 26-Jun-2024]. URL: https://www.hbkworld.com/en/knowledge/resource-center/articles/strain-measurement-basics/optical-strain-sensor-fundamentals/tips-for-configuring-optical-sensors#!ref_hbm.com.
- [4] Ramaswami Rajiv, Sivarajan Kumar N, Sasaki GH (Galen Hajime). *Optical networks a practical perspective*. 3rd ed. The Morgan Kaufmann series in networking. Amsterdam ; Elsevier/Morgan Kaufmann, 2010. ISBN: 9786612540936.
- [5] Kashyap Raman. *Fiber Bragg gratings*. 2nd ed. Amsterdam: Academic Press, 2010. ISBN: 9786612618154.
- [6] Hill KO, Meltz G. Fiber Bragg grating technology fundamentals and overview. *Journal of lightwave technology* 15.8 (1997), pp. 1263–1276. DOI: 10.1109/50.618320.
- [7] R. Paschotta. *Fresnel Reflections*. [Accessed: 9-Jan-2024]. URL: https://www.rp-photonics.com/fresnel_reflections.html.
- [8] R. Paschotta. *Bragg Mirrors*. [Accessed: 9-Jan-2024]. URL: https://www.rp-photonics.com/bragg_mirrors.html.
- [9] Erdogan, T. Fiber grating spectra. *Journal of Lightwave Technology* 15.8 (1997), pp. 1277–1294. DOI: 10.1109/50.618322.
- [10] Othonos A. Fiber Bragg gratings. *Review of scientific instruments* 68.12 (1997), pp. 4309–4341. DOI: 10.1063/1.1148392.
- [11] Toba M, Mustafa FM, Barakat TM. New simulation and analysis fiber Bragg grating: narrow bandwidth without side lobes. *Journal of physics communications* 4.7 (2020), pp. 1–13. DOI: 10.1088/2399-6528/ab0600.
- [12] Gemzicky E, Mullerova J. Analysis of Simulated Reflection Characteristics of Uniform and Apodized Fiber Bragg Gratings. *Advances in electrical and electronic engineering* 7.1-2 (2008), pp. 21–24. ISSN: 1336-1376.

- [13] Tosi D. Review of chirped fiber bragg grating (CFBG) fiber-optic sensors and their applications. *Sensors (Basel, Switzerland)* 18.7 (2018), pp. 2147–. DOI: 10.3390/s18072147.
- [14] HBK. *Tips for configuring an optical sensors' array*. [Accessed: 20-Mar-2024]. URL: https://www.hbkworld.com/en/knowledge/resource-center/articles/strain-measurement-basics/optical-strain-sensor-fundamentals/tips-for-configuring-optical-sensors#!ref_hbm.com.
- [15] Morozov O. *Fiber Bragg Grating Based Sensors and Systems*. Basel, Switzerland: MDPI - Multidisciplinary Digital Publishing Institute, 2021. ISBN: 9783036519067.
- [16] Gao H, Jiang Y, Cui Y, Zhang L, Jia J, Jiang L. Investigation on the Thermo-Optic Coefficient of Silica Fiber Within a Wide Temperature Range. *Journal of lightwave technology* 36.24 (2018), pp. 5881–5886. DOI: 10.1109/JLT.2018.2875941.
- [17] Lee HJ, Abdullah F, Emami SD, Ismail A. Fiber modeling and simulation of effective refractive index for tapered fiber with finite element method. *2016 IEEE 6th International Conference on Photonics (ICP)*. IEEE, 2016, pp. 1–3. DOI: 10.1109/ICP.2016.7509998.
- [18] Rollinson, C. M. *Microscopic and Spectral Characterisation of Optical Fibre Bragg Gratings [dissertation]*. 2012.
- [19] Méndez Alexis, Morse TF. *Specialty optical fibers handbook*. 1st edition. Oxford: Academic Press, 2007. ISBN: 9786611004095.
- [20] Hitachi A, Chepel V, Lopes MI, Solovov VN. New approach to the calculation of the refractive index of liquid and solid xenon. *The Journal of chemical physics* 123.23 (2005), pp. 234508–234508. DOI: 10.1063/1.2136879.
- [21] Albert J, Malo B, Hill KO, Bilodeau F, Johnson DC, Thériault S. Comparison of one-photon and two-photon effects in the photosensitivity of germanium-doped silica optical fibers exposed to intense ArF excimer laser pulses. *Applied physics letters* 67.24 (1995), pp. 3529–3531. DOI: 10.1063/1.114911.
- [22] Lemaire PJ, Watson HA, DiGiovanni DJ, Walker KL. Prediction of long-term hydrogen-induced loss increases in Er-doped amplifier fibers. *IEEE photonics technology letters* 5.2 (1993), pp. 214–217. DOI: 10.1109/68.196009.
- [23] Lemaire PJ. Reliability of optical fibers exposed to hydrogen: prediction of long-term loss increases. *Optical Engineering* 30.6 (1991), pp. 780–789. DOI: 10.1117/12.55865.
- [24] Masuda Y, Nakamura M, Komatsu C, Fujita K, Yamauchi M, Kimura M, et al. Wavelength evolution of fiber Bragg gratings fabricated from hydrogen-loaded optical fiber during annealing. *Journal of lightwave technology* 22.3 (2004), pp. 934–941. DOI: 10.1109/JLT.2004.825784.
- [25] Hill KO. Photosensitivity in optical fiber waveguides: from discovery to commercialization. *IEEE journal of selected topics in quantum electronics* 6.6 (2000), pp. 1186–1189. DOI: 10.1109/2944.902166.

- [26] Morey WW, Meltz G, Glenn WH. Holographically generated gratings in optical fibers. *eng. Optics and photonics news* 1.7 (1990), pp. 14–16. DOI: 10.1364/OPN.1.7.000014.
- [27] Meltz G, Morey WW, Glenn WH. Formation of Bragg gratings in optical fibers by a transverse holographic method. *Optics letters* 14.15 (1989), pp. 823–825. DOI: 10.1364/OL.14.000823.
- [28] Stone J. Interactions of hydrogen and deuterium with silica optical fibers: A review. *Journal of lightwave technology* 5.5 (1987), pp. 712–733. DOI: 10.1109/JLT.1987.1075562.
- [29] Hui Rongqing, O'Sullivan MS (Maurice S). *Fiber optic measurement techniques*. Amsterdam ; Elsevier/Academic Press, 2009. ISBN: 9786612286896.
- [30] Qin Q, Wang M, Rao B, Li H, Wang Z. Method for measuring reflectivity of weak reflection large-mode-area fiber Bragg gratings using scale gratings. *Optics express* 30.15 (2022), pp. 26472–26483. ISSN: 10.1364/OE.464255.
- [31] Optromix. *Fiber Optic Sensing: Fiber Bragg Grating Sensor Interrogation Systems*. [Accessed: 3-Mar-2024]. URL: <https://fibergratings.com/fiber-optic-sensing-fiber-bragg-grating-sensor-interrogation-systems/>.
- [32] Taylor John R. *Introduction to Error Analysis*. 2nd ed. Amsterdam: University Science Books,U.S., 1997. ISBN: 9780935702750.
- [33] Rana, K. P. S. et al. FPGA Implementation of Steinhart-Hart Equation for Accurate Thermistor Linearization. *IEEE sensors journal* 18.6 (2018), pp. 2260–2267. DOI: 10.1109/JSEN.2018.2795098.